AERODYNAMIC EFFECTS ON TWO-LANE RURAL HIGHWAY SAFETY

FINAL PROJECT REPORT

by

Ahmad A.A. Hammad and Tao Xing
Department of Mechanical Engineering
University of Idaho, Moscow, Idaho, USA

Sponsored by The Pacific Northwest Transportation Consortium (PacTrans), Region 10 University Transportation Center (UTC), U.S. Department of Transportation (USDOT)

for
Pacific Northwest Transportation Consortium (PacTrans)
USDOT University Transportation Center for Federal Region 10
University of Washington
More Hall 112, Box 352700
Seattle, WA 98195-2700

In cooperation with US Department of Transportation-Research and Innovative Technology Administration (RITA)

Disclaimer

The contents of this report reflect the views of the authors, who are responsible for the facts and the accuracy of the information presented herein. This document is disseminated under the sponsorship of the U.S. Department of Transportation's University Transportation Centers Program, in the interest of information exchange. The Pacific Northwest Transportation Consortium, the U.S. Government and matching sponsor assume no liability for the contents or use thereof.

Technical Report Documentation Page

1. Report No.	2. Government Accession No.	3. Recipient's Catalog No.	

4. Title and Subtitle Aerodynamic Effects on Two-Lane Rural Highway Safety	5. Report Date 14 August 2017
	6. Performing Organization Code
7. Author(s) Ahmad A.A. Hammad and Tao Xing	8. Performing Organization Report No.
9. Performing Organization Name and Address PacTrans Pacific Northwest Transportation Consortium University Transportation Center for Region 10 University of Washington More Hall 112 Seattle, WA 98195-2700	10. Work Unit No. (TRAIS)
	11. Contract or Grant No. DTRT13-G-UTC40
12. Sponsoring Organization Name and Address United States of America Department of Transportation Research and Innovative Technology Administration	13. Type of Report and Period Covered Research
	14. Sponsoring Agency Code

15. Supplementary Notes
Report uploaded at www.pacTrans.org

16. Abstract

Two-lane rural highways experience a higher rate of traffic accidents than to other types of highways. One factor affecting this rate is the impact of aerodynamics on a vehicle's stability and safety during crossing and overtaking maneuvers, especially under adverse environmental conditions such as crosswinds. This study investigated this phenomenon by using three-dimensional, unsteady computation fluid dynamics (CFD) simulations, with validation from wind tunnel experiments. The forces and moments acting on the vehicles were analyzed, and experiments showed that the forces acting on a vehicle may increase by up to 9 times, with the maximum increase associated with a size discrepancy between the vehicles. The presence of crosswinds increased the variations in fluctuations of forces and moments. To evaluate existing highway policies, additional parametric studies are needed to fully investigate the impacts of different crosswind speeds and directions, as well as different lateral distances between vehicles during crossing and overtaking maneuvers.

17. Key Words Vehicle aerodynamics, CFD, vehicle safety, wind tunnel	18. Distribution Statement No restrictions.	
19. Security Classification (of this report) Unclassified.	20. Security Classification (of this page) Unclassified.	21. No. of Pages	22. Price NA

Form DOT F 1700.7 (8-72) **Reproduction of completed page authorized**

Table of Contents

List of Figures

List of Tables

Acknowledgments

This project was supported by the Pacific Northwest Consortium and the National Institute for Advanced Transportation Technology (NIATT). The authors would like to thank NIATT's director, Professor Abdel-Rahim, for his valuable input to the project, and in particular, his continuous moral, personal and professional support during the past two years. Additionally, we must thank the Mechanical Engineering Department at the University of Idaho. Using the wind tunnel facilities in the department was only one small part of their contribution: wherever we went, there was always a member of the Department—a student, professor or staff member—eager to work with us, assist us, or think creatively with us, all the way to the conclusion of this project.

Executive Summary

Vehicle safety on two-lane rural roads is an issue of paramount importance, given the disproportionate number of fatalities on these kinds of roads. This study investigated aerodynamic effects on vehicle safety by using three-dimensional transient computational fluid dynamics (CFD) simulations and experimental wind tunnel validation. The forces and moments acting on cars and trucks were analyzed under different scenarios, including crossing and overtaking maneuvers and with consideration for the effects of crosswinds.

Analysis of the simulations in this study showed that vehicles aerodynamically influence each other for a longer duration than the time it takes for them to cross or overtake each other. It also showed that a larger vehicle, such as a truck, interacts in a complex manner with a smaller vehicle, such as a car, causing fluctuations in the magnitude and direction of lateral aerodynamic forces acting on the car (increasing by up to 9 times), as well as affecting longitudinal forces and yaw and roll moments. However, the duration of these force fluctuations is too small to create a significant impulse on any of the vehicles involved or affect their stability.

Chapter 1 Introduction

Rural roads in the U.S., in comparison to urban roads, experience a proportionately higher number of fatalities with respect to traffic volume. This risk is most apparent on two-lane, undivided rural highways shared by fast-moving cars and trucks, especially on twisty sections of these roads where winds are more variable in terms of speed and direction. These vehicles impose aerodynamic forces and moments on one another, and the significance of these forces and moments on vehicle stability has increased with the trend toward lighter, more fuel-efficient vehicles.

Studies investigating the aerodynamics of vehicle interaction and their effect on safety have suffered from shortcomings that include use of two-dimensional models, unsuitable modeling assumptions, coarse grids, and low temporal resolution; the absence of rigorous verification and validation; and a lack of parametric studies involving different wind conditions and different distances separating vehicles. This study used three-dimensional computational fluid dynamics (CFD) models and wind tunnel experimental measurements to investigate vehicle interactions and the variations in forces and moments associated with them, especially when the size differences between two vehicles is large, as is the case between cars and trucks. High resolution grids were used in all simulations, as well as the appropriate turbulence models, to resolve all flow structures. This study aimed to influence safety policies on two-lane highways in terms of safe lateral and trailing distances, especially in the presence of variable environmental wind conditions.

Chapter 2 Literature Review

In an overtaking or crossing maneuver on a highway involving two vehicles, the flow fields around the two vehicles interact generating transient aerodynamic forces that can affect car handling and stability [1]. When the relative size difference between the two vehicles is large (e.g., between a car and a truck), these forces increase on the smaller vehicle, and they increase even further under the influence of crosswinds, especially when the overtaking car is on the leeside of the truck [2]. A vehicle is more stable when its geometric center, center of gravity, and stagnation point are all in line. Under crosswind, the air flow around the vehicle becomes asymmetric, and the stagnation point shifts towards the direction of the crosswind, affecting the stability of the vehicle [3]. As the computational power of commercially available computers has doubled approximately every two years (famously observed and predicted by Gordon Moore [4]), high quality transient computational fluid dynamics (CFD) simulations of the complex interactions between moving vehicles have not been feasible until the late 2000s. This literature review is divided into three sections that are based on the physics of the study (single vehicles, vehicle interaction, and vehicle interaction in the presence of crosswinds).

2.1 Single Vehicle (Car/Truck)

Tsubokura *et al.* [5] conducted full-scale simulations on a *single* passenger car by using a Large Eddy Simulation (LES) model that could reproduce unsteady turbulence characteristics with high accuracy. The simulation used about 38 million cells, and the resulting vortices and flow structures were visualized in detail and validated with full-scale wind tunnel experiments. The yaw angle of the vehicle was also changed, to mimic sudden crosswinds, and the change in the flow structures was investigated. The study showed the advantages of using LES to provide aerodynamic data on the different eddy structures around vehicles in comparison to conventional wind tunnel tests or Reynolds-Averaged Navier-Stokes (RANS) simulations. A later study by

Tsubokura *et al.* [6] investigated the aerodynamic response to transient crosswinds of a 5 percent scale model passenger car by using LES and wind tunnel experiments validation. Unsteady and gusty crosswinds were considered in the study, showing all six components of aerodynamic forces and moments in each case.

Sterken *et al*. [7] used the realizable k-ε turbulence model with standard wall functions and 90 million cells to investigate the wake-shape behind a passenger car. The moving ground and rotating wheels were simulated. Full-scale models were used for both the simulations and the experimental studies, and there was good correlation between them in terms of drag coefficient. The wake-shape showed both similarities and differences.

2.2 Crossing/Overtaking Maneuvers between Vehicles

Using a sliding mesh method, Wang *et al*. [8] conducted a three-dimensional CFD study on the transient aerodynamic forces occurring on a motorcycle overtaken by a truck, considering three different lateral distances between the two vehicles. Results showed the variation in forces and moments on the motorcycle during the overtaking process. However, the simulation used the Reynolds-Averaged Navier-Stokes (RANS) model and only 1.7 million computational cells. This model experienced difficulties capturing unsteady flow characteristics [5]. No experimental studies were performed to validate the results.

A study by Al Homoud *et al*. [9] conducted CFD simulations on a car overtaking a truck by using full-scale geometries. It did not mention the turbulence model used in the simulations, and there was no experimental validation. The results did not show the variation of forces acting on the car with time, as the study followed a quasi-steady approach. Zhang *et al*. [10] conducted a transient CFD study on two vehicles crossing each other by using k-ε turbulence model; however, it is not clear whether the geometries used were two-dimensional (2-D) or three-dimensional (3-D). There was no experimental validation for the results.

Basara *et al*. [12], using a hybrid RANS/LES scheme (denoted as PANS, Partially Averaged Navier-Stokes [11]) to perform CFD simulations on a car overtaking a truck, showed that the drag on the car increased to its maximum value when the car reached the front of the truck. The result was validated by experimental studies using 40 percent scaled models of both vehicles, fixed at eight relative positions between the two models, thus approximating the unsteady process with a quasi-steady process. This increase in forces on the overtaking vehicle as it approached the front of the overtaken vehicle was corroborated by similar experimental studies conducted by Howell *et al*., performed at a 12.5 percent scale [2]. This wind tunnel study used a stepper motor and a system of cables and pulleys to simulate the overtaking maneuver between two vehicles (a truck and a car) for a range of yaw angles (-10^{o} to $+10^{o}$) and a range of lateral separating distances. It estimated the incremental loads generated in such a maneuver, showing that these loads increased in the presence of a crosswind when the car was on the leeside of the truck.

A three-dimensional, CFD, quasi-steady study on a car overtaking a truck by Pasala *et al*. [13] assumed that the relative velocity between two vehicles has a negligible effect on the flow distribution and the forces acting on the car. This study lacked experimental validation.

Existing literature data are inconclusive regarding the effects of overtaking velocity when the size difference between the two vehicles is significantly large (e.g., a car overtaking a truck). It is suggested that the absolute velocity of the larger vehicle is dominant in determining the loads on the smaller vehicle [2]. However, according to Shrefl *et al*. [14], on the basis of an on-road experiment, the lateral loads on a car overtaking a truck tend to increase linearly with the overtaking velocity.

Simulations of the dynamic passing process between generic vehicles (Ahmed bodies) were conducted by Uystepruyst and Krajnović [15] by using the URANS model and studying

changes in the force and moment coefficients of the overtaken vehicle. However, the Ahmed bluff body was too simplified to be able to provide a basis for drawing quantitative conclusions from these simulations.

Experimental wind tunnel studies were conducted by Noger *et al*. [16] to study the transient aerodynamic forces and moments associated with overtaking maneuvers. Vehicle models at 20 percent scale were used, and the two vehicles had similar size. However, the geometries used were very simplified rectangular bluff bodies. Results showed that these forces and moments changed considerably with the lateral spacing between the two cars. Interestingly, the crosswind effects did not generate new unsteady effects for either car.

Kremheller [17] measured the surface pressure distribution of a passenger car during both an overtaking and a passing maneuver in instrumented experiments on a proving ground. These experiments showed that the asymmetric pressure distribution induced by these maneuvers influenced lateral acceleration and yawing rates, being pronounced in vehicles with a larger frontal area. The change in surface pressure increased when the lateral distance between vehicles decreased. A good correlation between CFD and experimental data was found; however, only a brief explanation of the comparison between CFD results and experimental measurements was presented in this paper.

A CFD and experimental study conducted in 2015 by Blocken *et al*. [18] investigated the influence of a car on the drag coefficient of a cyclist being *followed* by that car, at different separating distances. While this study did not investigate aerodynamic effects during car/bicycle crossing and overtaking, it showed the importance of the effects of a larger vehicle closely following a much smaller one, and the non-linear response of the drag coefficient of the smaller vehicle as the larger vehicle closed in.

2.3 Vehicle Interaction in the Presence of Crosswinds

In 2008, Corin *et al.* [1] also performed simulations during an overtaking maneuver between two similarly sized vehicles under crosswinds. Quasi-steady and unsteady simulations were performed, and with the latter, the dynamic variation in the aerodynamic forces for the overtaken vehicle was up to 150 percent greater than that predicted by quasi-steady analysis, and up to 400 percent greater in crosswind conditions, indicating the unsuitability of the quasi-steady approach in modelling overtaking maneuvers. This discrepancy was most noticeable when the relative velocity between the two vehicles was higher than 20 percent of the overtaken vehicle's velocity. However, this study used simplified, 2-D car geometries in a coarse grid with approximately 50,000 cells. Experimental wind tunnel testing was conducted statically on each of the models in isolation for validation. The experimental results showed the difficulty of accurately predicting complex, unsteady turbulent flow structures with CFD, especially as the one-equation Spalart–Allmaras (SA) model, which has a dissipative Reynolds-averaging nature, was employed in the simulations.

Altinisik *et al*. [3] performed an experimental study on a 20 percent scale passenger car model, for a single car at various yaw angles (0-40 degrees), and for a two-vehicle platoon at 3 different vehicle spacings. The experimental study was performed in two wind tunnels to investigate the effect of blockage on aerodynamic coefficients. The experimental results detailed the static pressure distributions on the surface of the car, showing that the maximum drag coefficient was at a yaw angle of 35^{o}, with drag decreasing at larger angles. They also showed that drag on the leading car in a two-vehicle platoon decreased with decreasing separating distance between the two cars. Three-dimensional, unsteady CFD simulations, using a realizable k-ε turbulence model, were also conducted to supplement the experimental results and agreed favorably with them.

In summary, to the best of our knowledge, previous studies in this area have had one or more of the following limitations:

a) use of 2-D geometries;

b) low grid resolutions;

c) inappropriate turbulence models that were too dissipative, destroying details of the important vortical structures in the flow; and

d) absence lack of rigorous verification and validation (V&V) or use of qualitative measurements.

To address these concerns, our CFD study of vehicle interaction used the following:

a) 3-D, model scale geometries of vehicles;

b) fine grids with up to 9 million grid points; and

c) use of the Improved Delayed Detached Eddy Simulation (IDDES) turbulence model, a hybrid RANS/LES model that accurately resolves small flow structures near the solid boundaries of the vehicles and larger flow structures farther away from the boundaries, while avoiding grid-induced separation of the boundary layer.

d) Limitation (d) was partially addressed by using the finest grid we could afford and conducting accurate experimental tests on a single model-scale car and truck to validate our simulations.

On the basis of the velocity of air relative to the vehicle u, the length of the vehicle L, and the kinematic viscosity of air ν, the vehicles in our study had a lower Reynolds number ($\mathrm{Re}=uL/\nu = 4\times10^5$ to 1.1×10^6) than actual road conditions (greater than 1×10^7), thanks to using model-scale vehicles in this study. This was necessitated by the need to validate simulation results by model-scale experimental studies in the wind tunnel.

Chapter 3 Method

This chapter describes the process of setting up our CFD simulations, as well as the experimental wind tunnel study procedure. All simulations involving the passenger car and truck were run at 1:25 scale. Experiments involving the car were also performed on a 1:25 scale model; however, the truck model was smaller at 1:37.5 scale because of size constraints inside the wind tunnel test section.

3.1 CFD Methodology

3.1.1 Car Geometry

A generic passenger car model designed in SolidWorks was used (fig. 3.1). It was designed on the basis of the average dimensions of mid-size family sedans in the US market (e.g., Toyota Camry, Honda Accord, Ford Fusion, etc), in terms of overall length, height, width, track width and wheelbase length. Other important proportions (cabin length, beltline height, etc.) were also in line with typical mid-size sedans.

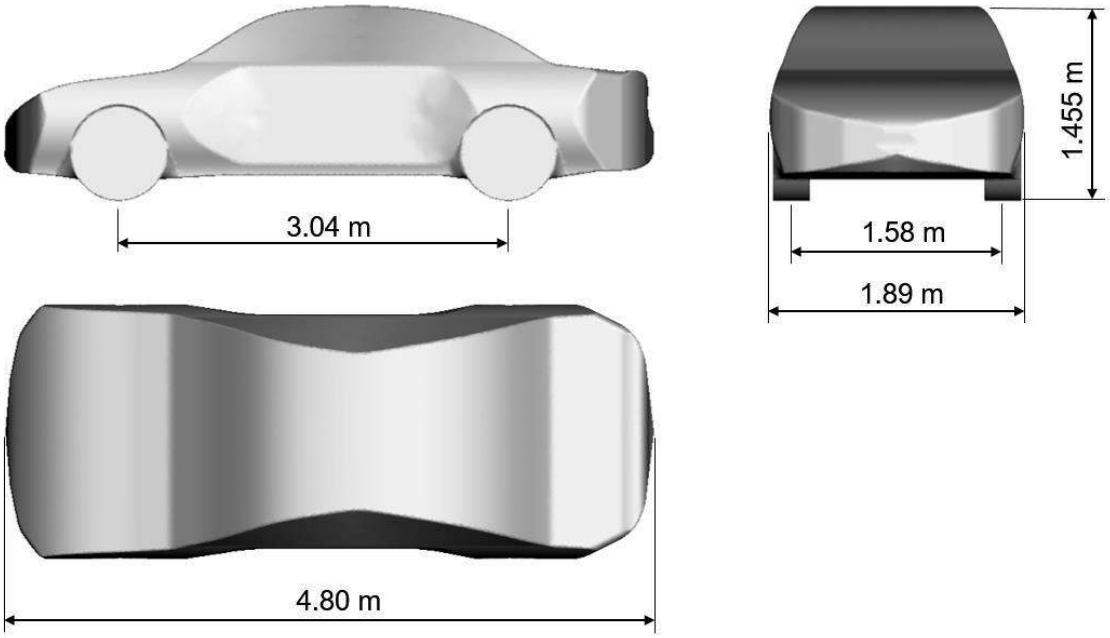

Figure 3.1 Major dimensions of the passenger car model (true dimensions)

The vehicle lacked a wheel gap between the wheels and the fenders, and wheel motion was not considered in this study.

3.1.2 Truck Geometry

The semi-trailer truck (fig. 3.2) consisted of a cab-over tractor unit attached to a 9.75 m semi-trailer with three axles, based on a Volvo model that was simplified (by omitting surface textures such as the grill, headlights, windows, etc.) to be more generic. This simplification also streamlined the mesh generation process.

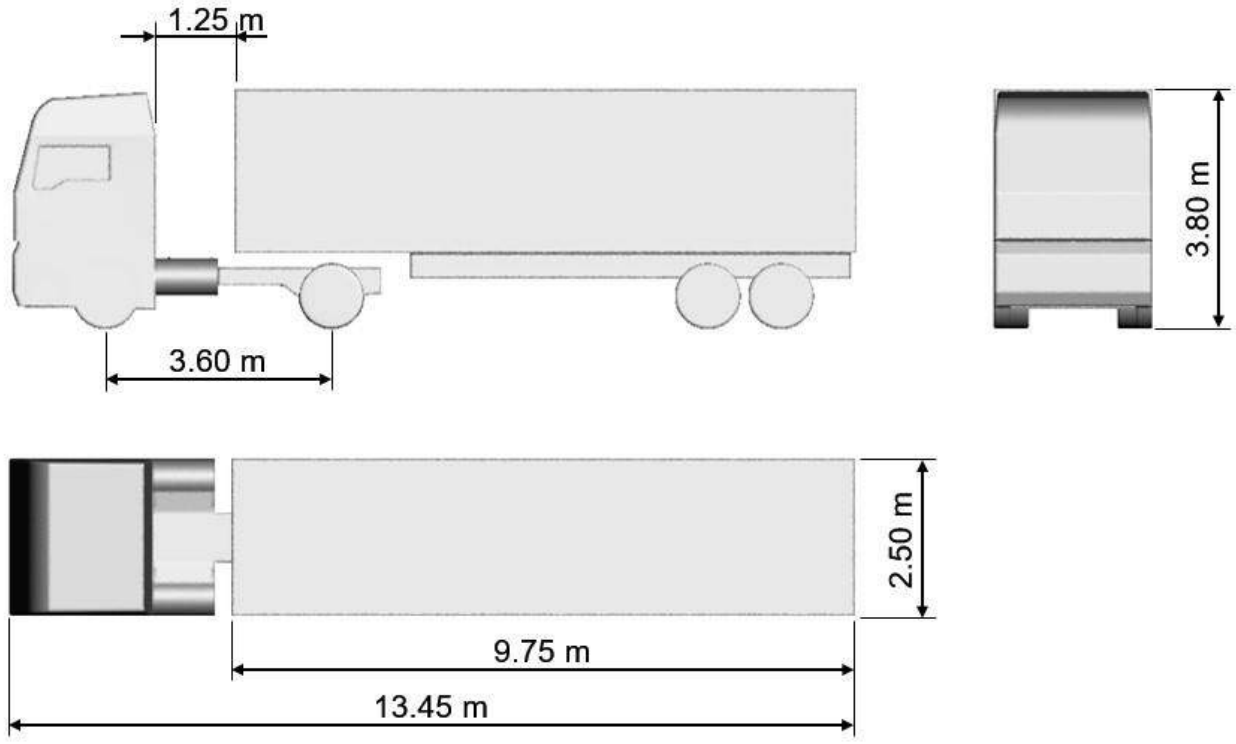

Figure 3.2 Major dimensions of the semi-trailer truck model

Table 3.1 Model-scale vehicle dimensions in simulations

Dimensions	Passenger car	Truck
Total length (m)	0.192	0.538
Wheelbase (m)	0.122	0.144
Width (m)	0.076	0.100
Height (m)	0.058	0.152
Front/rear track (m)	0.063	0.091/0.079
Frontal area (m^2)	0.004408	0.0152

3.1.3 Grid Topology and Simulation Design

The dimensions of the vehicles were scaled down to percent of their original sizes so that CFD results could be directly validated by experimental results of 1:25 vehicle models in the wind tunnel. Commercial mesh generating software, Pointwise (V17.2R3), was used to generate the mesh. The grid topologies are essentially the same for both the car and truck. An unstructured grid was used on the surfaces of the vehicles. The volume immediate to the vehicle surfaces was filled with structured, triangular-aspect prisms (fig. 3.3) to provide adequate grid points to resolve the boundary layer.

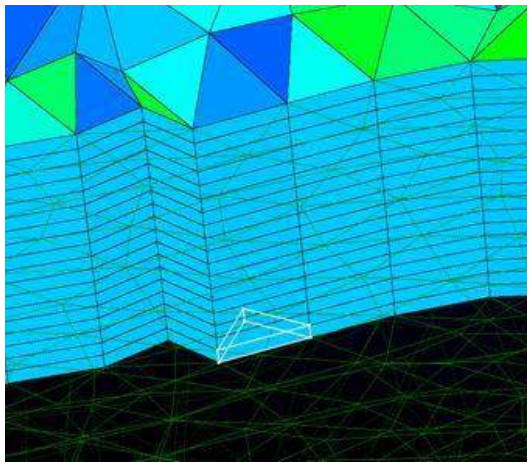

Figure 3.3 Triangular prisms in the boundary layer close to the car surface. The first grid point away from the wall was at a distance of 1e-5 m, for an approximate y^+ value of 2.

The volume between these cells and the inner surfaces of a cuboid containing each vehicle was populated with unstructured, pyramid-shaped cells. The dynamic mesh zones behind and in front of each vehicle were structured and of very high resolution, and they consisted of cuboids: ($X \times Y \times Z$) 0.004×0.004×0.004m in simulations containing passenger cars only, and 0.004×0.005×0.004m in simulations involving trucks (fig. 3.4, fig. 3.5.)

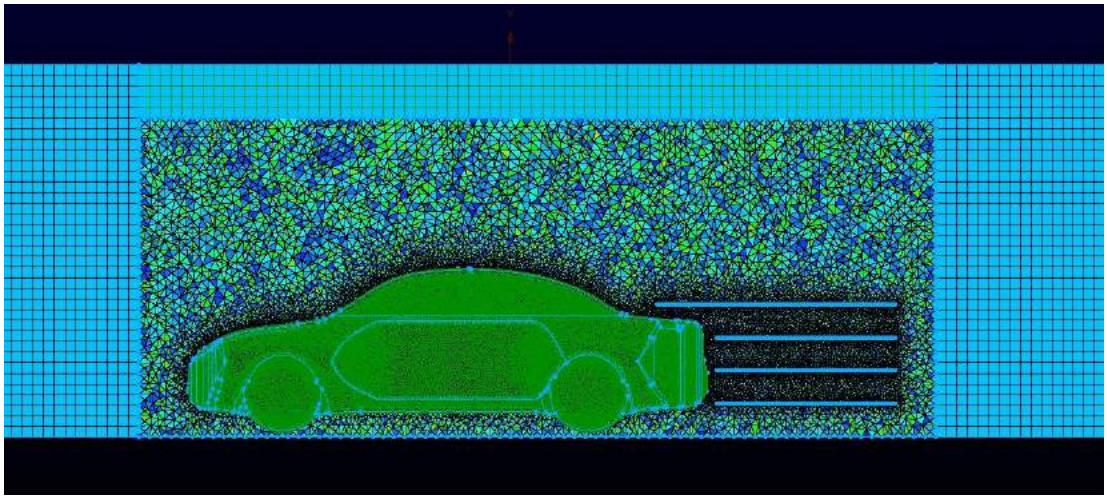

Figure 3.4 A slice through the mesh showing the unstructured grid surrounding the car, and the structured zones further away from it.

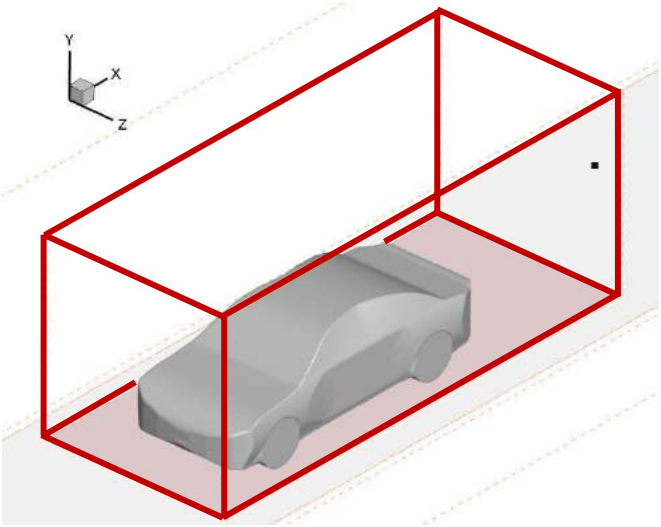

Figure 3.5 The red boundary outlines the unstructured zone around the car.

A large, rectangular, low-resolution zone enclosed the dynamic mesh zones (fig. 3.6) The lateral distance separating the two vehicles was approximately a half-lane wide (1.6 m).

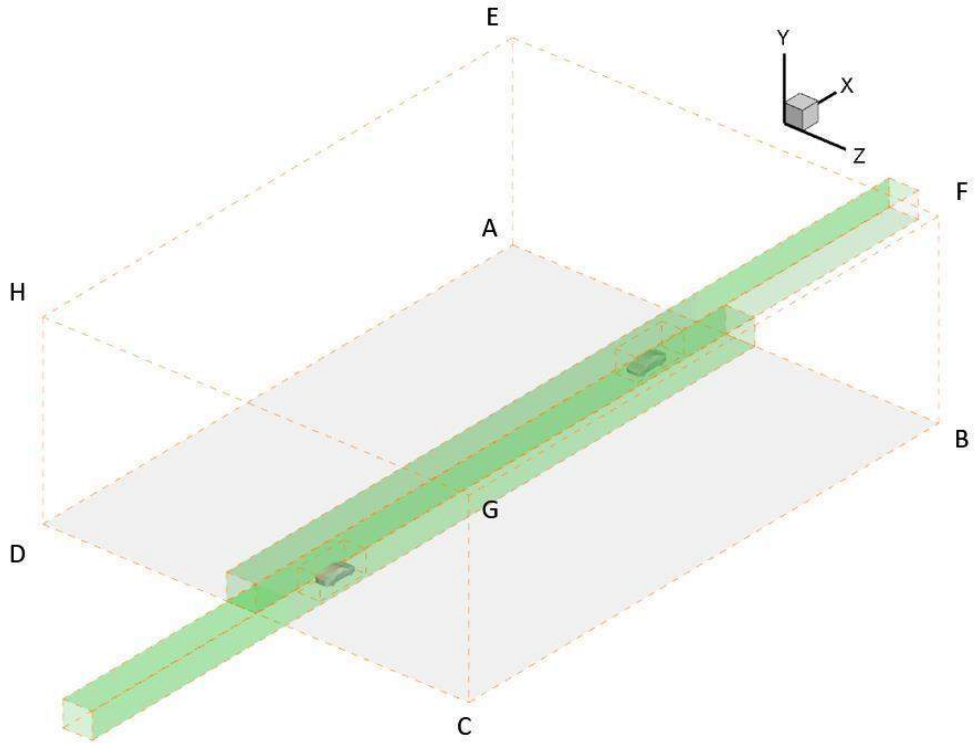

Figure 3.6 Set-up of the case of two cars crossing each other.
The initial separating distance between the cars was 10 car lengths. The green zones containing the vehicles slid against each other at 30 m/s to simulate the crossing.

In simulations of vehicles crossing each other, the velocity of each vehicle was 30 m/s (67 mph), corresponding to a Reynolds number (based on vehicle length) of 4×10^5 for the passenger car, and 1.1×10^6 for the semi-trailer truck. In simulations of overtaking maneuvers, the truck was moving at 30 m/s, and the car was 6 m/s (13.22 mph) faster. The overall simulation matrix with and without crosswinds is summarized in table 3.2.

Table 3.2 Simulation matrix, in the presence or absence of crosswinds

Simulation		Re	No. of points (millions)	Initial separating distance (m, at 1:25 scale)
Car-car (crossing)	No crosswinds	4×10^5	7.1	2.0 (10 car lengths)
	Crosswinds	4.5×10^5		
Car-truck (crossing)	No crosswinds	1.1×10^6	9.0	5.4 (27 car lengths)
	Crosswinds	1.27×10^6		
Car-truck (overtaking)	No crosswinds	1.1×10^6	7.4	2.0 (10 car lengths)
	Crosswinds	1.27×10^6		
Single car	No crosswinds	4×10^5	2.2	N/A
	Crosswinds	4.5×10^5		
Single truck	No crosswinds	4×10^5	3.0	N/A
	Crosswinds	4.5×10^5		

3.1.4 Numerical Method

The commercial CFD software ANSYS Fluent 17.1 and 17.2 was used in the simulations, using a least squares cell-based discretization method and a transient solver. The SIMPLE algorithm was used for the pressure-velocity coupling. A second order scheme was used for pressure discretization. The momentum equations were discretized by using bounded central differencing. An implicit second order scheme was used for temporal discretization.

3.1.5 Dynamic Mesh Method

The sliding mesh model in Fluent was used to simulate the relative motion between the vehicles involved. This model is a special case of general dynamic mesh motion wherein the nodes move rigidly in a given dynamic mesh zone, i.e., all of the boundaries and the cells of a given mesh zone move together in a rigid-body motion. In this situation, the nodes of the mesh move in space (relative to the fixed, global coordinates), but the cells defined by the nodes (the zones behind and in front of the vehicles) do not deform [19]. Furthermore, mesh zones moving

adjacent to one another are linked across non-conformal interfaces (the zones separating the imaginary "tunnels" in which the vehicles move relative to one another, and the zones separating these tunnels and the larger zone enclosing them), which allows for fluid flow from one mesh to the other [19].

3.1.6 Turbulence Model

In all simulations in this study, the flow around the vehicles involved was predicted by using the Improved Delayed Detached-Eddy Simulation "IDDES" [20], which combines Delayed Detached-Eddy Simulation "DDES" [21] with an improved RANS-LES hybrid model. This model surpasses both DES and DDES in simulating mixed flows with both attached and separated regions. DES (Detached-Eddy Simulation, Spalart *et al*., 1997) and its modification, Delayed DES, are models developed with the aim of accurately predicting massively separated flows at a manageable computational cost [22]. DES combines RANS (ReynoldsAveraged Navier-Stokes equations) in the attached boundary layers, which are populated with small eddies that have a length-scale much less than the boundary layer thickness (δ), with LES (Large-Eddy Simulation) in the complex, massively separated regions away from the wall, where large, unsteady turbulent scales play a dominant role. DES can produce artificial separation of the boundary layer, in an effect termed Grid Induced Separation (GIS) [23], when the switch from RANS to LES happens inside the boundary layer as a result of a refinement in the grid in that region [24].

3.1.6.1 Governing Equations

The incompressible continuity and momentum equations for Cartesian coordinates read as follows [25]:

$$\boldsymbol{\nabla} \cdot (\rho \boldsymbol{V}) = 0 \tag{3.1}$$

$$\frac{\partial}{\partial t}(\rho V) + \nabla \cdot (\rho V^2) =$$
$$-\boldsymbol{\nabla} p + \boldsymbol{\nabla} \cdot [\mu(\boldsymbol{\nabla V} + \boldsymbol{\nabla V}^{\mathrm{T}})] + \rho \boldsymbol{g} \tag{3.2}$$

where $\boldsymbol{V}$ is the velocity vector, ρ is the density, μ is the dynamic viscosity, p is the pressure and $\boldsymbol{g}$ is gravitational acceleration.

RANS equations in Cartesian tensor form are given by:

$$\frac{\partial \rho}{\partial t} + \frac{\partial \rho}{\partial x_i}(\rho u_i) = 0 \tag{3.3}$$

$$\frac{\partial}{\partial t}(\rho u_i) + \frac{\partial}{\partial x_j}(\rho u_i u_j) = -\frac{\partial \rho}{\partial x_j} + \frac{\partial}{\partial x_j}\left[\mu\left(\frac{\partial u_i}{\partial x_j} + \frac{\partial u_j}{\partial x_i} - \frac{2}{3}\delta_{ij}\frac{\partial u_l}{\partial x_l}\right)\right] + \frac{\partial}{\partial x_j}(-\rho\overline{u_i u_j}) \tag{3.4}$$

where $u_i = u_i + u'_i$, and u_i and u'_i, are the mean and fluctuating velocity components.

Because of the aforementioned shortcomings of using the RANS model for massively separated flows, this study followed the SST IDDES formulation published by Gritskevich *et al*. [23]. IDDES is a hybrid RANS-LES model, based on the baseline/standard (BSL/ST) model.

SST IDDES formulation: Transport equations for k and ω:

$$\frac{\partial \rho k}{\partial t} + \boldsymbol{\nabla} \cdot (\bar{\rho} U k) = \boldsymbol{\nabla} \cdot [(\mu + \sigma_k \mu_t)\boldsymbol{\nabla} k] + P_k - \frac{\rho\sqrt{k^3}}{l_{IDDES}} \tag{3.5}$$

$$\frac{\partial \rho \omega}{\partial t} + \boldsymbol{\nabla} \cdot (\bar{\rho} U \omega) = \boldsymbol{\nabla} \cdot [(\mu + \sigma_\omega \mu_t)\boldsymbol{\nabla}\omega] + 2(1 - F_1)\rho\sigma_{k_2}\frac{\nabla k \cdot \nabla \omega}{\omega} + \alpha\frac{\rho}{\mu_t}P_k - \beta\rho\omega^2 \tag{3.6}$$

where k is the turbulence kinetic energy, ω is the specific dissipation rate, P_k is the production term, and F_1 and F_2 are the SST blending functions defined in equations 3.8 and 3.9.

$$\mu_t = \rho\frac{a_1 \cdot k}{\max(a_1 \cdot \omega, F_2 \cdot S)} \tag{3.7}$$

where S is the magnitude of the strain rate tensor and $a_1 = 0.31$

$$F_1 = \tanh(\arg_1^4) \tag{3.8}$$

$$\arg_1 = \min\left(\max\left(\frac{\sqrt{k}}{C_\mu \omega d_\omega}, \frac{500v}{d_\omega{}^2 \omega}\right), \frac{4\rho\sigma_{\omega_2} k}{CD_{k\omega} d_\omega{}^2}\right)$$

$$CD_{k\omega} = \max\left(2\rho\sigma_{\omega_2} \frac{\nabla k \cdot \nabla \omega}{\omega}, 10^{-10}\right)$$

$$F_2 = \tanh(\arg_2^2) \tag{3.9}$$

$$\arg_1 = \min\left(\max\left(\frac{\sqrt{k}}{C_\mu \omega d_\omega}, \frac{500v}{d_\omega{}^2 \omega}\right), \frac{4\rho\sigma_{\omega_2} k}{CD_{k\omega} d_\omega{}^2}\right)$$

arg2 $C_\mu \omega d_\omega \, d\omega 2\omega$

$$\arg_2 = \max\left(\frac{2\sqrt{k}}{C_\mu \omega d_\omega}, \frac{500v}{d_\omega{}^2 \omega}\right)$$

where d_ω is the distance to the nearest wall and other model constants are: $C_\mu = 0.09$, $\alpha_1 = 5/9$, $\beta_1 = 0.075$, $\sigma_{k1} = 0.85$, $\sigma_{\omega 1} = 0.5$, $\alpha_2 = 0.44$, $\beta_2 = 0.0828$, $\sigma_{k2} = 1$, and $\sigma_{\omega 2} = 0.856$. The production term in 3.6 is calculated using:

$$P_k = \min(\mu_t S^2, 10 \cdot C_\mu \rho k \omega) \tag{3.10}$$

The IDDES length-scale is defined by using the following:

$$l_{IDDES} = \tilde{f}_d \cdot (1 + f_e) \cdot l_{RANS} + (1 - \tilde{f}_d) \cdot l_{LES}$$

$$l_{LES} = C_{DES} \Delta \tag{3.11}$$

$$l_{RANS} = \frac{\sqrt{k}}{C_\mu \omega}$$

$$C_{DES} = C_{DES1} \cdot F_1 + C_{DES2} \cdot (1 - F_1) \tag{3.12}$$

$l = \sqrt{k}$

$$\Delta = \min\{C_w \max[d_w, h_{\max}], h_{\max}\} \tag{3.13}$$

where Δ is the LES length-scale, h_{max} is the maximum edge length of the cell, $C_{DES1} = 0.78$, and $C_{DES2} = 0.61$. The empiric blending function $\tilde{f}_d$ is computed by using the following:

$$\tilde{f}_d = \max\{(1 - f_{dt}), f_b\} \tag{3.14}$$

$$f_{dt} = 1 - \tanh[(C_{dt1} \cdot r_{dt})^{C_{dt2}}]$$

$$r_{dt} = \frac{\nu_t}{\kappa^2 d_w^2 \sqrt{0.5(S^2 + \Omega^2)}}$$

$$f_b = \min\{2\exp(-9\alpha^2), 1.0\}$$

$$\alpha = 0.25 - d_\omega / h_{max} \tag{3.15}$$

where $\kappa = 0.41$, Ω is the magnitude of the vorticity tensor, and the elevation function f_e is defined by using the following:

$$f_e = f_{e2} \cdot \max((f_{e1} - 1.0), 0.0) \tag{3.16}$$

$$f_{e1} = \begin{cases} 2 \cdot exp(-11.09 \cdot \alpha^2), \alpha \geq 0 \\ 2 \cdot exp(-9.0 \cdot \alpha^2), \alpha < 0 \end{cases}$$

$$f_{e2} = 1.0 - \max(f_t, f_l)$$

$$f_t = \tanh((C_t^2 \cdot r_{dt})^3)$$

$$f_l = \tanh((C_t^2 \cdot r_{dl})^{10})$$

$$r_{dl} = \frac{\nu}{\kappa^2 d_w^2 \sqrt{0.5(S^2 + \Omega^2)}} \tag{3.17}$$

Other constants introduced in this model are $C_w = 0.15$, $C_{dt1} = 20$, $C_{dt2} = 3$, $C_l = 5.0$ and $C_t = 1.87$.

3.1.7 Boundary and Initial Conditions

The faces of the large rectangular zone surrounding the dynamic mesh zones had different boundary conditions depending on the scenario. See table 3.3 and figure 3.7 for a description of those boundary conditions.

Table 3.3 Boundary conditions

Faces			Boundary conditions
ABCD	All cases		Slip wall
EFGH	All cases		Slip wall
ABFE	No crosswinds	Car-car (crossing) Car-truck (crossing) Car-truck (overtaking)	Constant pressure outlet
	Crosswinds	Car-car (crossing) Car-truck (crossing)	Slip wall
DCGH	No crosswinds	Car-car (crossing) Car-truck (crossing)	Constant pressure outlet
		Car-truck (overtaking)	Constant velocity inlet
	Crosswinds	Car-car (crossing) Car-truck (crossing)	Slip wall
ADHE, BCGF	No crosswinds	Car-car (crossing) Car-truck (crossing)	Constant pressure outlet
		Car-truck (overtaking)	Slip wall
	Crosswinds	Car-car (crossing) Car-truck (crossing)	Constant velocity inlet (17.32 m/s to simulate 30^{o} crosswind)

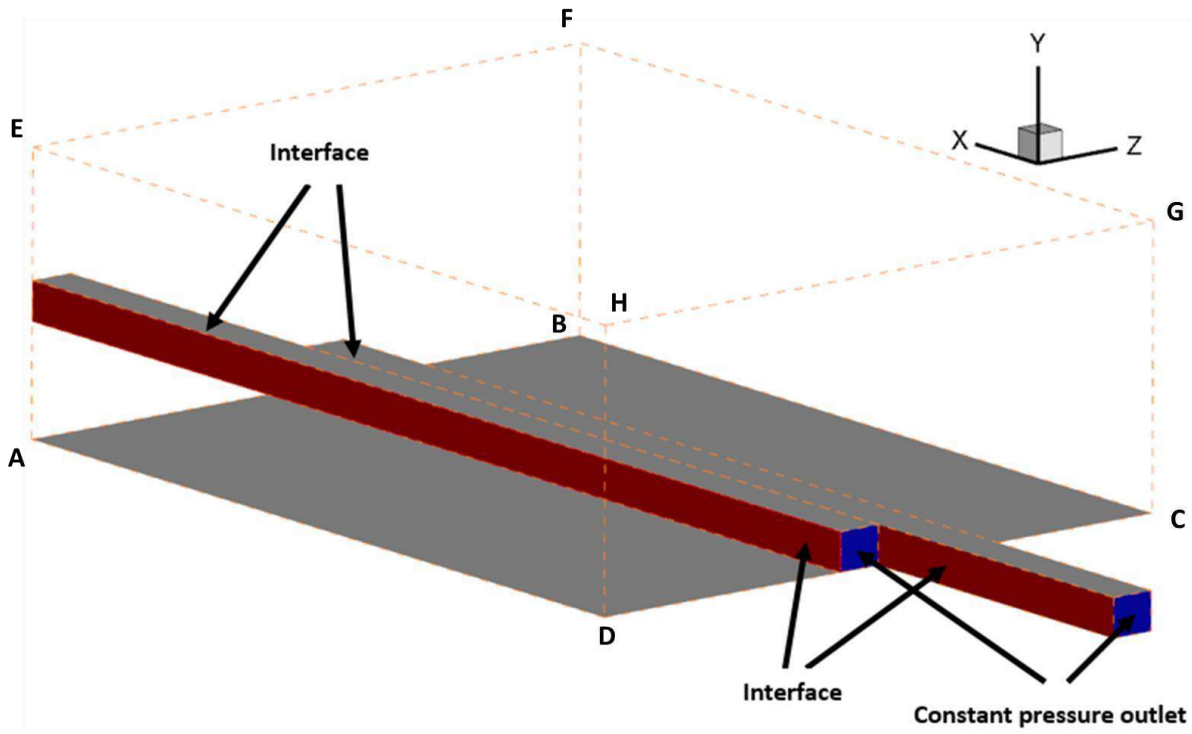

Figure 3.7 Boundary conditions

Pressure-outlet parameters*:*

Gauge pressure = 0

Backflow turbulent intensity = 1 percent

Backflow turbulent viscosity ratio = 0.1

3.1.8 CFD Analysis Method

In each simulation, forces and moments acting on the vehicle surfaces were recorded at each time step. These forces and moments were non-dimensionalized to form *coefficients by* using the following formulas:

$$Force\ coefficient = \frac{2F}{\rho u^2 A}$$

$$Moment\ coefficient = \frac{2M}{\rho u^2 A L} \quad (3.18)$$

where

F and *M* are the force (N) and moment (Nm), respectively,

ρ is the air density (1.225 kg/m^3), u is the relative velocity magnitude of air with respect to the vehicle (m/s),

A is the frontal area of the vehicle (m^2) (0.04408 m^2 and 0.0152 m^2 for the car and truck respectively), and

L is the total length of the vehicle (m).

Fast Fourier Transform (FFT) analysis was conducted on the time histories of forces to identify their power spectrum. The frequencies of different vortical structures could then be associated with the FFT analysis.

The flow around the vehicles, and in particular the shedding vortices, were visualized by using the isosurfaces of *Q*-Criterion: in an incompressible flow, a vortex is a connected fluid region with a positive second invariant of ∇u, where the vorticity magnitude is greater than the magnitude of rate of strain:

$$Q = \frac{1}{2}(u_{i,j}^2 - u_{i,j}u_{j,i}) = -\frac{1}{2}u_{i,j}u_{j,i} = \frac{1}{2}(\|\Omega\|^2 - \|S\|^2) > 0 \quad (3.19)$$

where Q represents the local balance between shear strain rate and vorticity magnitude. This criterion also requires the pressure to be lower than the ambient pressure in the vortex [26, 27].

3.2 Experimental Methodology

The purpose of the experiments was to measure the drag forces on a single, 1:25 car model (Re = 4×10^5) and a single, 1:37.5 truck model (Re = 1.1×10^6). The drag force was used to validate a 3-D unsteady simulation of the same geometries for each vehicle individually. The subsonic wind tunnel in the Department of Mechanical Engineering at the University of Idaho was used to conduct the experiments, and the vehicle models were 3-D-printed at the department's facilities, with the necessary attachments manufactured in the machine shop (fig. 3.8.). The force balance was calibrated by using standard weights.

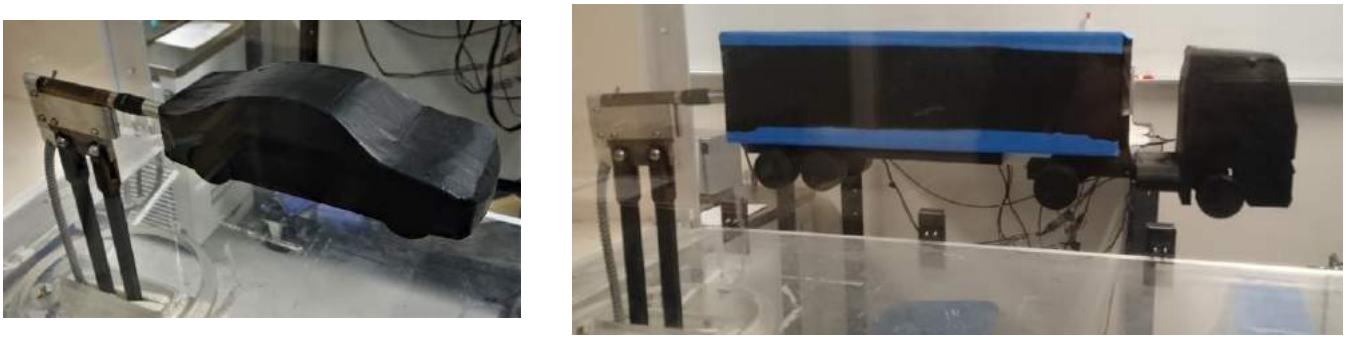

Figure 3.8 Experimental set-up inside the Mechanical Engineering wind tunnel

For each experimental run, after waiting 1 minute for the air velocity to stabilize, the researchers acquired a 5-second data sample by using a data acquisition device (fig. 3.9). The wind tunnel came to a complete stop before the next run began.

Figure 3.9 National instruments USB-6002 data acquisition system

The ir velocity inside the wind tunnel was changed by adjusting the variable-speed drive frequency. The frontal area of each vehicle (car = 0.004408 m^2, truck = 0.0152 m^2) was used to calculate the drag coefficient in each experimental run.

Chapter 4 Results and Discussion

4.1 Vehicle Interaction Scenarios in the Absence of Crosswinds

4.1.1 Experimental Validation of the Simulation Results

4.1.1.1 Experimental Validation of the Car Model

The wind tunnel experimental results for a single passenger car clustered around an average C_d value of 0.282. The variability in each test run was small, with a maximum standard deviation of about 1 percent of the average value in test no. 1. The CFD results were in good agreement with the experimental results. The uncertainty in each drag force measurement after wind tunnel calibration was less than 3 percent.

The aerodynamic blockage inside the wind tunnel was corrected by using the formula proposed by Sykes [28]:

$$w = 1 - mB \tag{4.1}$$

where w is the blockage correction factor, m is an empirical constant ($m=1.22$ as suggested by Stafford [29]), and B is the blockage ratio, defined as follows:

$$B = \frac{A_m}{A_w} \tag{4.2}$$

where A_m and A_w are the model frontal area and wind tunnel cross-sectional area, respectively. The corrected drag coefficient was defined by using the formula:

$$C_{dc} = wC_{dm} \tag{4.3}$$

where C_{dc} and C_{dm} are the corrected and measured drag coefficients, respectively. Altinisik *et al.* [30] suggested that for blockage ratios of less than 5 percent, the blockage correction method proposed by Sykes is one of three methods that give the most accurate results. The blockage ratio, B, of the passenger car inside the wind tunnel was 2 percent.

The CFD simulation results for the average normalized drag forces acting on the car model before it interacted with the other vehicle are shown alongside the experimental results in figure 4.1. The CFD results ranged from 1 percent lower up to 14 percent higher than the measurements. The CFD case that agreed most with measurements was the car overtaking truck, likely because in that case, the two vehicles were stationary during the initial part of the simulation, before the car started moving to overtake the truck, giving the flow more time to stabilize. This was facilitated by the fact that the two vehicles were moving in the same direction in this scenario. However, in the other two CFD cases, the two vehicles were always moving during the simulation, since it was impossible to prescribe an inlet velocity for two vehicles moving in opposite directions. The two vehicles were separated by a certain distance at the start of each simulation. This distance was limited by the computational affordability of CFD simulations; a single run of a simulation with a separating distance large enough to mimic the car overtaking the truck would take up to four months.

The discrepancy between the two other cases (two cars crossing, car-truck crossing) can be attributed to the same factor: in the simulation of two cars crossing, the separating distance between the two vehicles at the start of the simulation was 10 car lengths. This ensured that forces and moments reached quasi-stable states before the interaction between the vehicles started. This condition was satisfied in the simulation, but in comparison with the car-truck crossing case, the drag coefficient of the car in the latter case decreased gradually to a lower value, decreasing the average C_d value before interaction. This slow decline was an inadvertent side effect of having a much larger separating distance (27 car lengths) between the car and the truck at the start of the simulation. The larger distance was an adaptation to the larger size of the truck, which would start to influence the car aerodynamically at a longer distance.

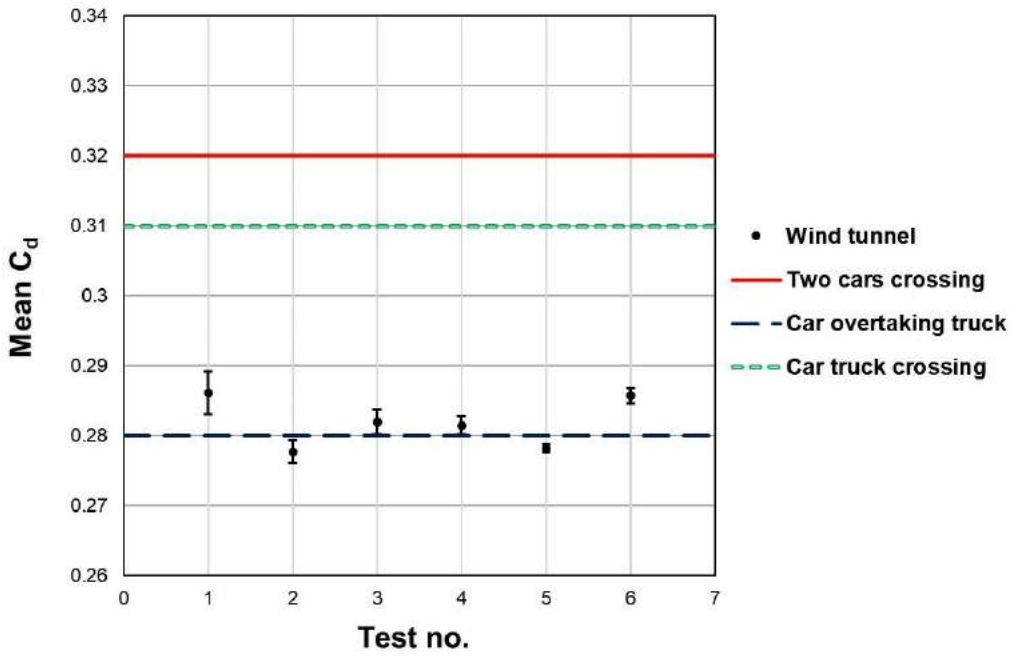

Figure 4.1 Experimental validation of a single car drag coefficient without crosswinds. Test samples, at 1000 Hz, were of the normalized drag forces acting on the passenger car model mounted inside the wind tunnel (Re = 4×10^5). Lines represent the average normalized drag forces acting on the same passenger car before it interacted with the other vehicle, in each of three simulations.

4.1.1.2 Experimental Validation of the Truck Model

The C_d value obtained from experimental measurements of the truck model had an average value of 0.855 (fig. 4.2). This is 26 percent higher than the simulation results and can be attributed to the following factors:

(a) The roughness and irregularity of the experimental truck model in comparison to the smooth truck surface considered in simulations. Results from simulations involving a truck were obtained before the truck model was created, precluding the possibility of including surface roughness in the simulations.

(b) The absence of ground effects in the experiments. In simulations, the vehicles were very close to the "ground" to simulate a road surface as realistically as possible.

However, in the wind tunnel, the experimental set-up placed the vehicle models approximately in the middle of the wind tunnel test section.

(c) Turbulence models. The IDDES model used in the CFD simulations is designed to simulate massively separated flows with good accuracy and relatively low computational effect; however, it is possible that turbulence models would not accurately predict transitional flows that might be present along the surfaces of the trailer of the truck.

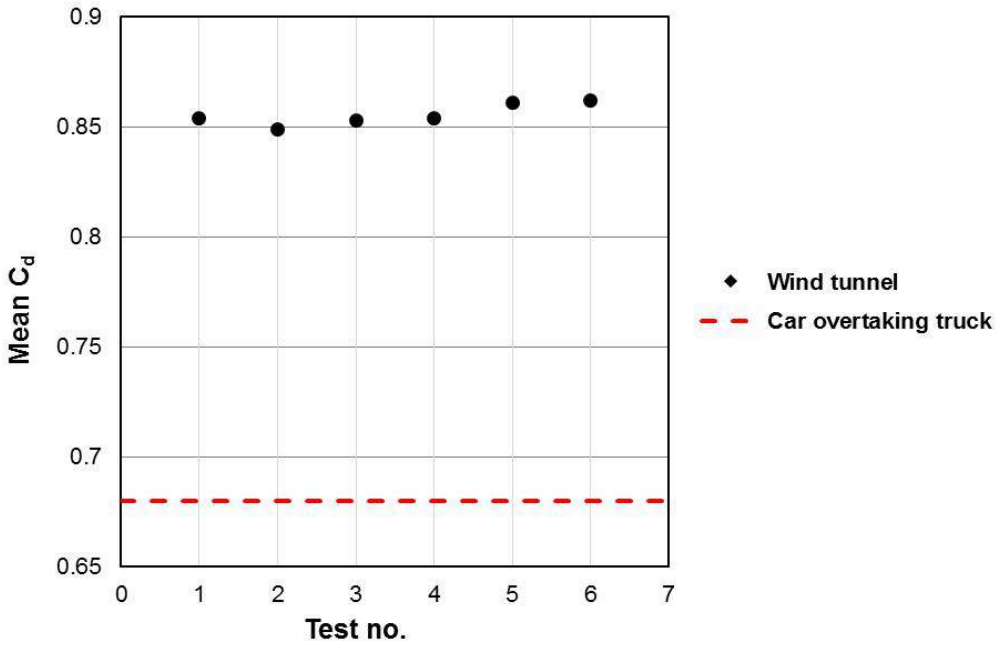

Figure 4.2 Experimental validation of a single truck drag coefficient without crosswinds. Normalized drag force measurements of the truck model mounted inside the wind tunnel ($Re=1.1\times10^6$). The dashed line represents the average normalized drag forces acting on the truck model in the CFD case.

4.1.2 Two Cars Crossing

4.1.2.1. Before Interaction between the Two Vehicles Started

The vortical structures in the airflow surrounding Car 1 can be seen figure 4.3. Vortices 1, 2, and 3 (fig. 4.3 (a)) were shed along the sharp roofline along each side of the car. They were

visually dominant, but they were always stable before interaction. Along each side, these three vortices broke down toward the end of the roofline, forming two top vortices in the wake of the car. The asymmetry of the periods of similar vortices located on the left and right sides of the car is explained by location of the stagnation pressure point (fig. 4.4). This point was slightly shifted away—on the horizontal plane—from the symmetry plane of the car, indicating that the incoming airflow impacted the car at an angle that was not exactly perpendicular.

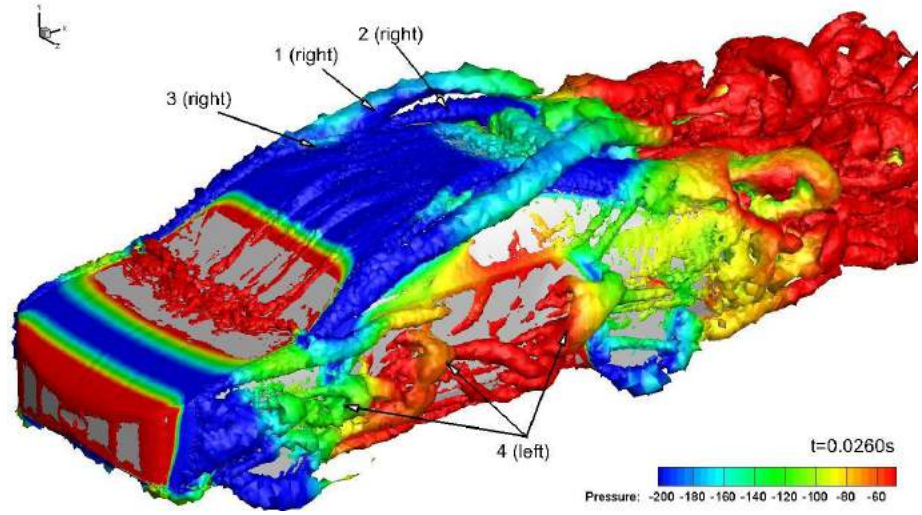

(a)

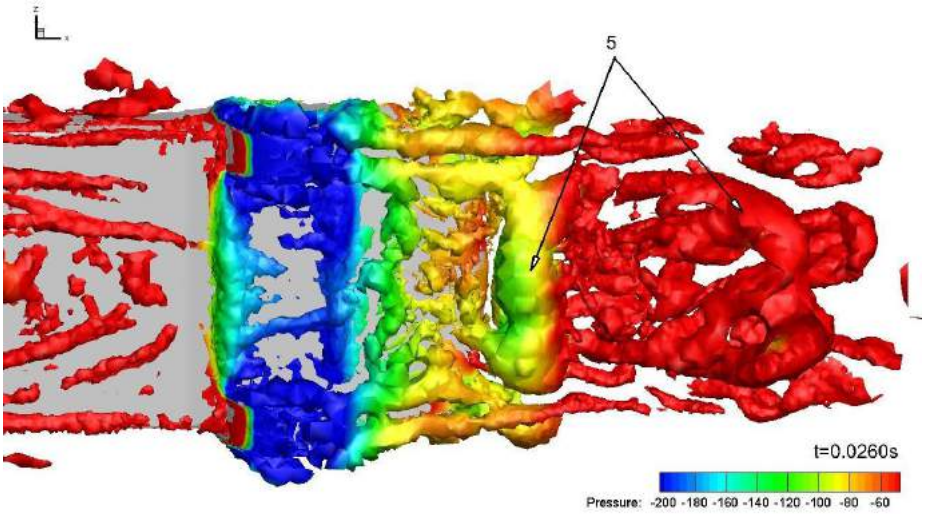

(b)

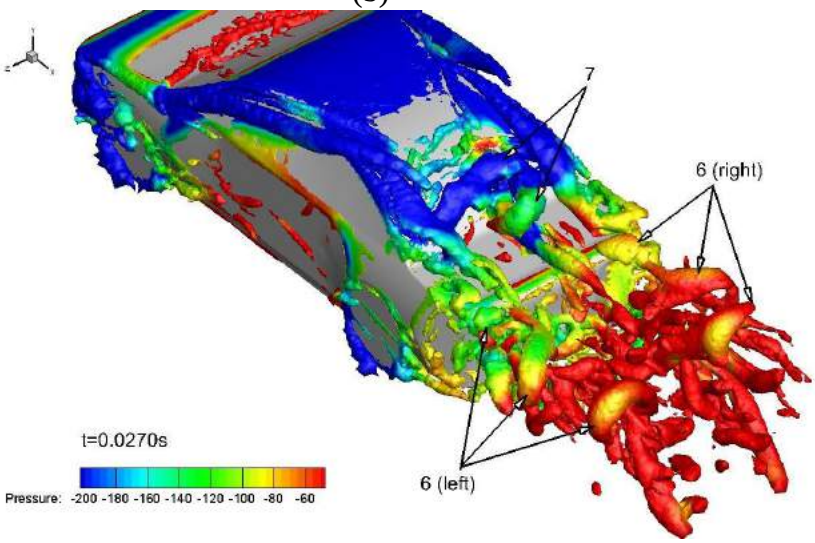

(c)

Figure 4.3 Defining vortical structures using isosurfaces of the Q-criterion

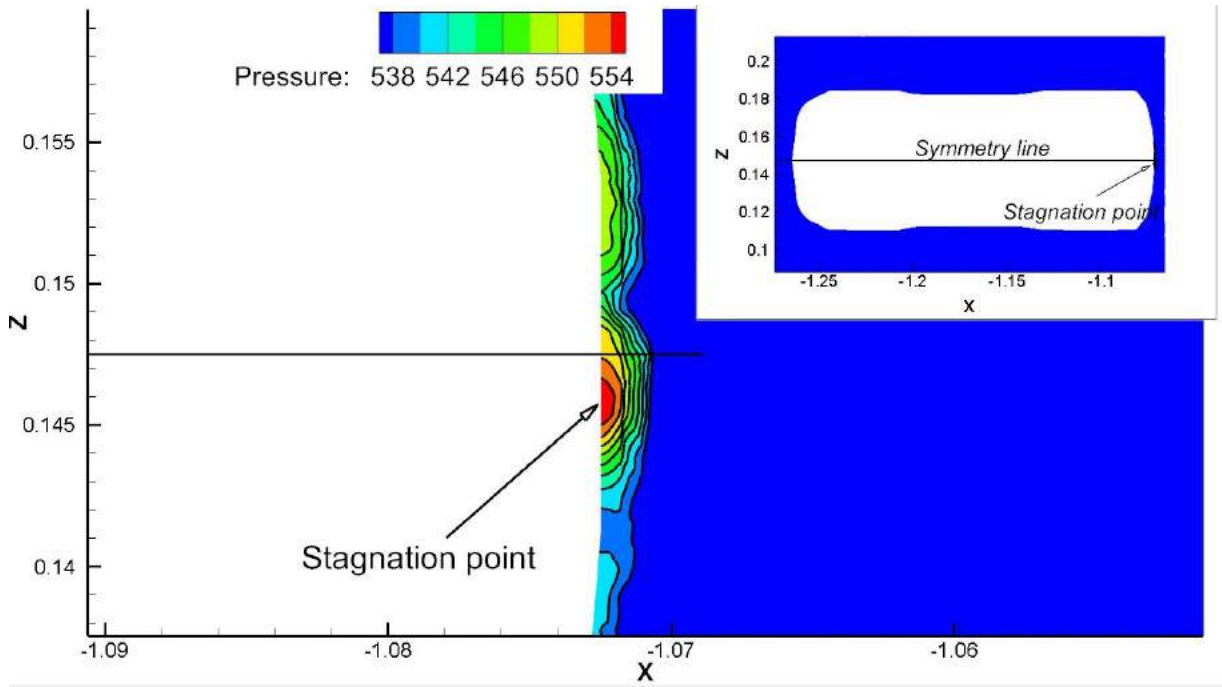

Figure 4.4 Horizontal slice through the car, highlighting the shifted position of the stagnation point at the front of the car

Spectral analysis of the drag coefficient during the pre-interaction period (0.015-0.045s), (/ig. 4.5) showed dominant frequencies at 100, 170, 200, and 300 Hz, each corresponding to the shedding frequency of one or more vortices.

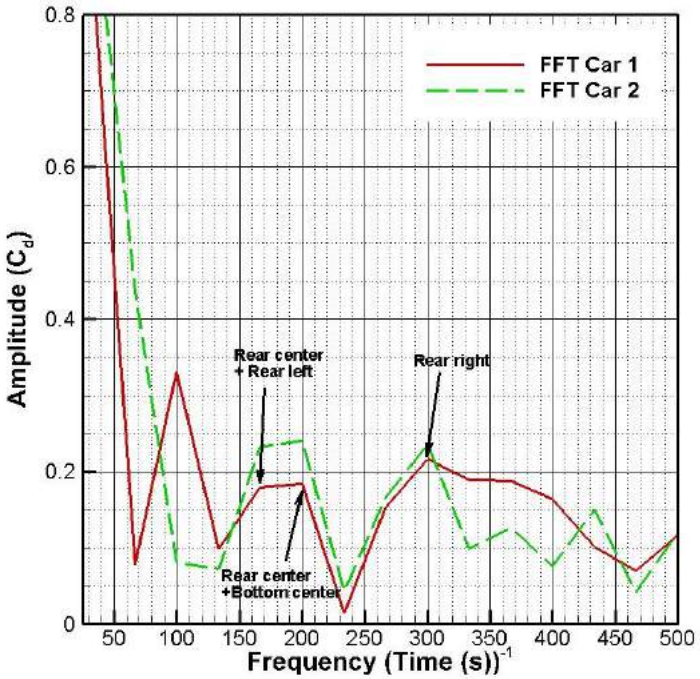

Figure 4.5 FFT analysis of drag coefficient before vehicle interaction

The rear top center vortex (vortex 7) was influenced by the two inner roofline vortices (2 and 3). This resulted in a complicated shedding pattern dominated by two frequencies (163, 192 Hz). At 0.0276s (fig. 4.6), a massive vortex spanning the width of the car started shedding, while further downstream of it a small helical vortex is present. This pattern was repeated starting at 0.0328s.

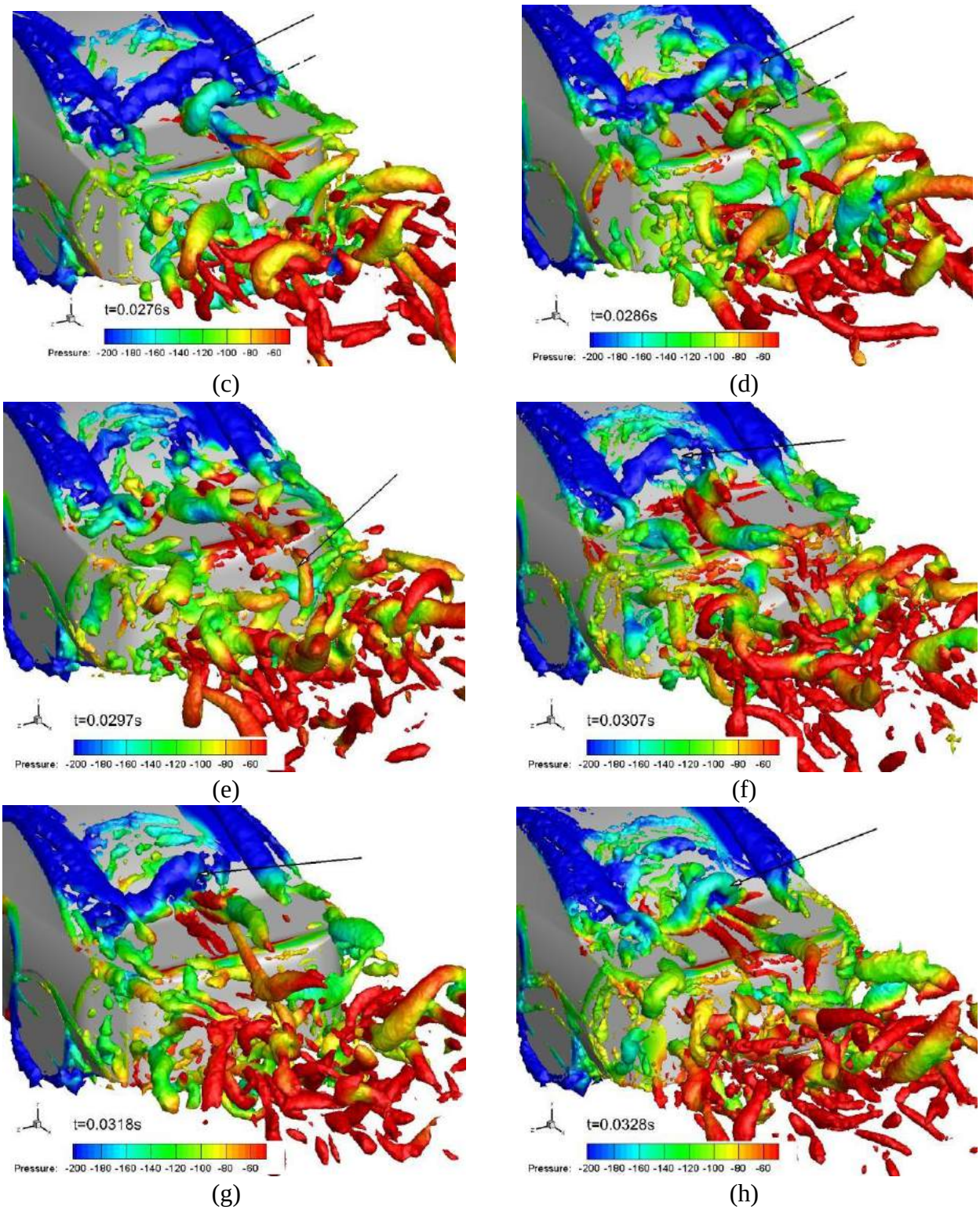

Figure 4.6 Rear center vortex (fig. 4.3 (c), vortex 7), showing isosurfaces of Q-criterion = $\mathbf{5e6}$
The shedding frequency (corresponding to fluctuations in drag coefficient) alternated between ~170 and ~200 Hz.

The other two rear top vortices (vortices 6 (right) and 6 (left)), haf different shedding frequencies, (159 and 294 Hz for the left and right sided vortices, respectively). Figure 4.7 and figure 4.8 show the progression of each vortex, shedding from the top edge of the trunk, then joined by the longitudinal vortex 1 after it broke down to form helical, counter-rotating vortical structures. Figure 4.9 and figure 4.10 show the asymmetrical side helical vortices. The left-side vortex had a much higher frequency (435 Hz) than the right-side vortex (~170 Hz). This left-side vortex also contributed to the formation of the left-side rear vortex.

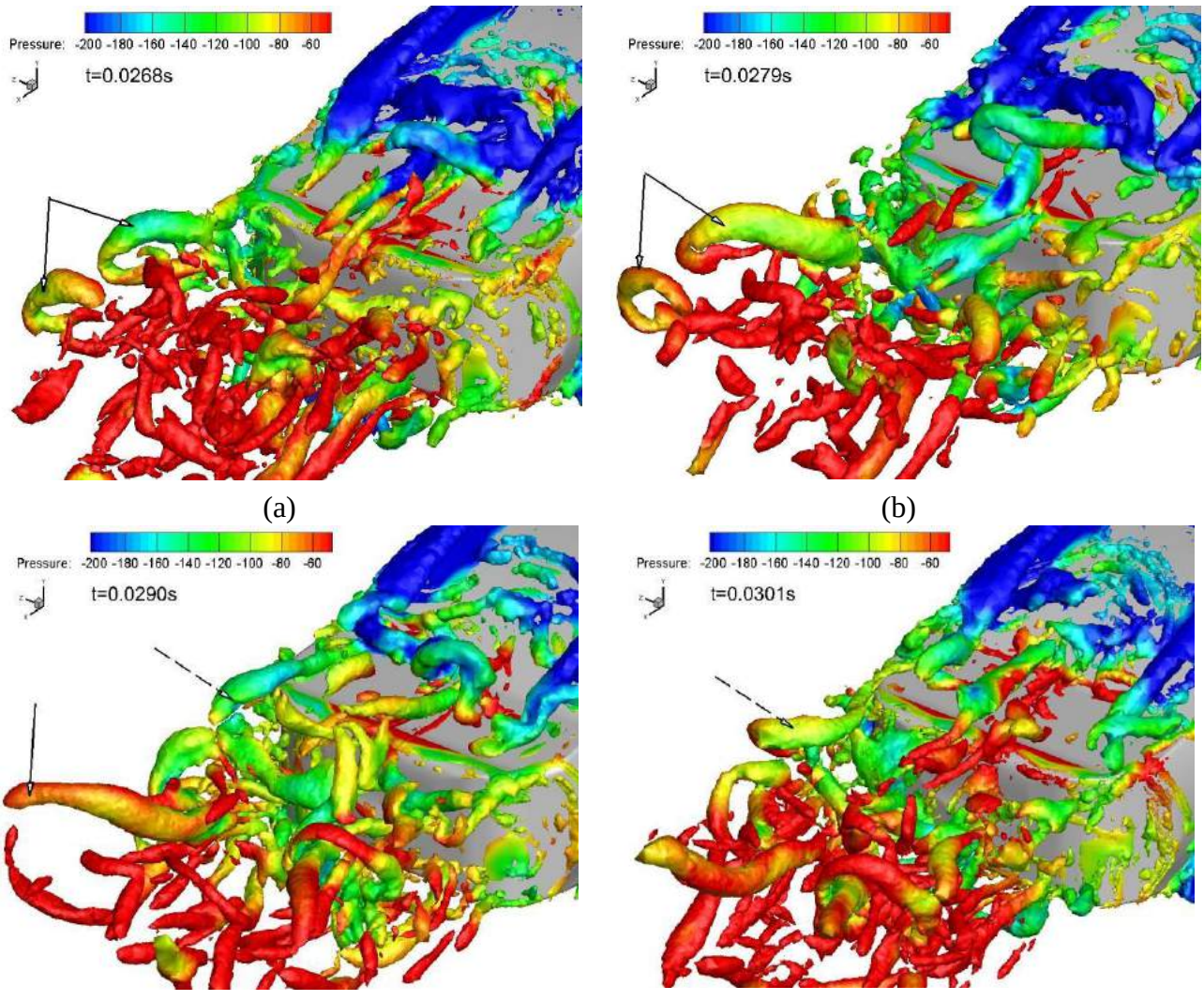

(a) (b)

(c) (d)

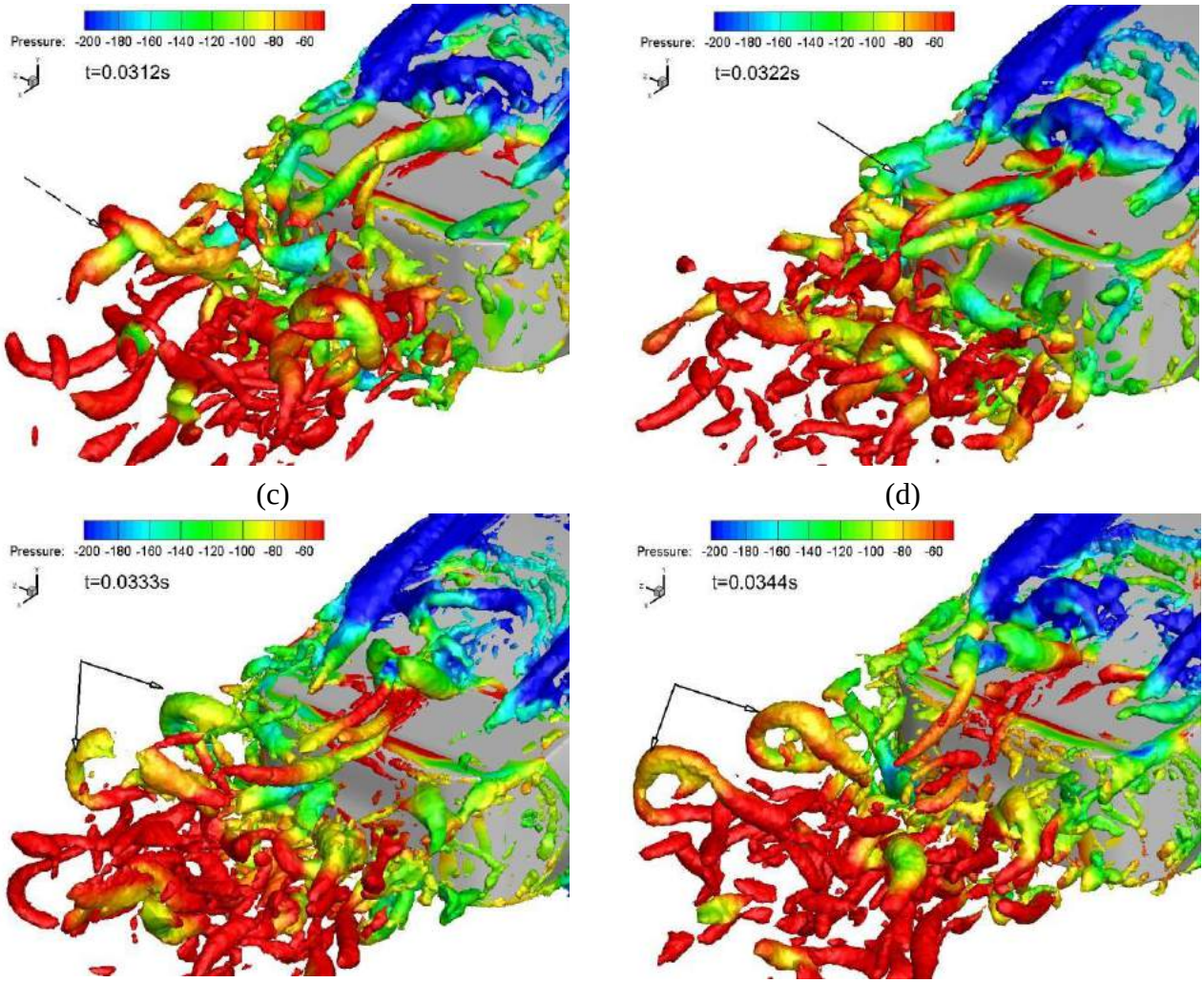

Figure 4.7 Rear left vortex (vortex 6), showing isosurfaces of Q-criterion $= \mathbf{5e6}$.
The shedding frequency of this vortex (~150 Hz) was different than its equivalent vortex at the other side of the car.

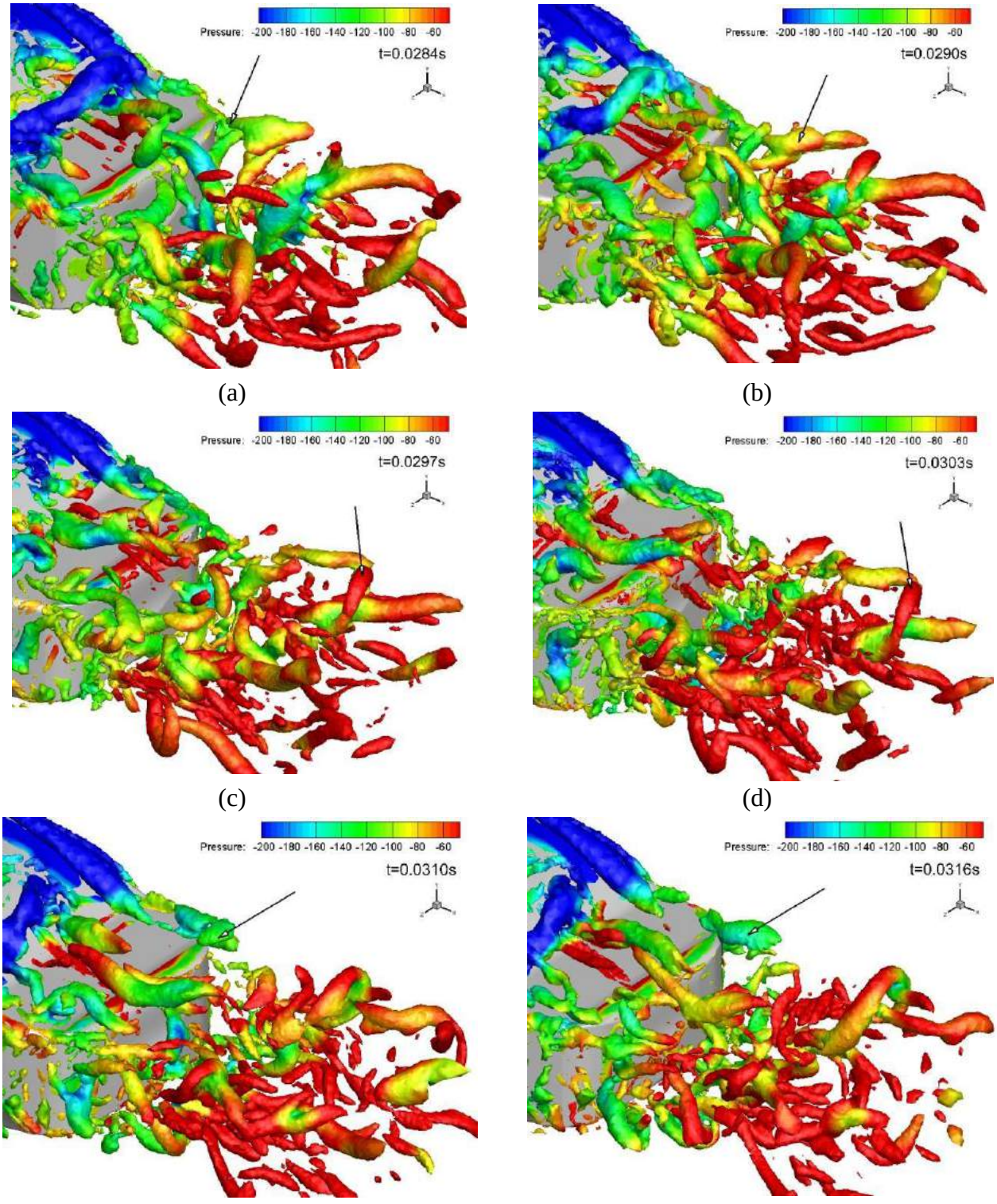

Figure 4.8 Rear right vortex (vortex 6), showing isosurfaces of Q-criterion = $\mathbf{5e6}$
It had twice the shedding frequency of its equivalent on the right side (~300 Hz in comparison to 150Hz).

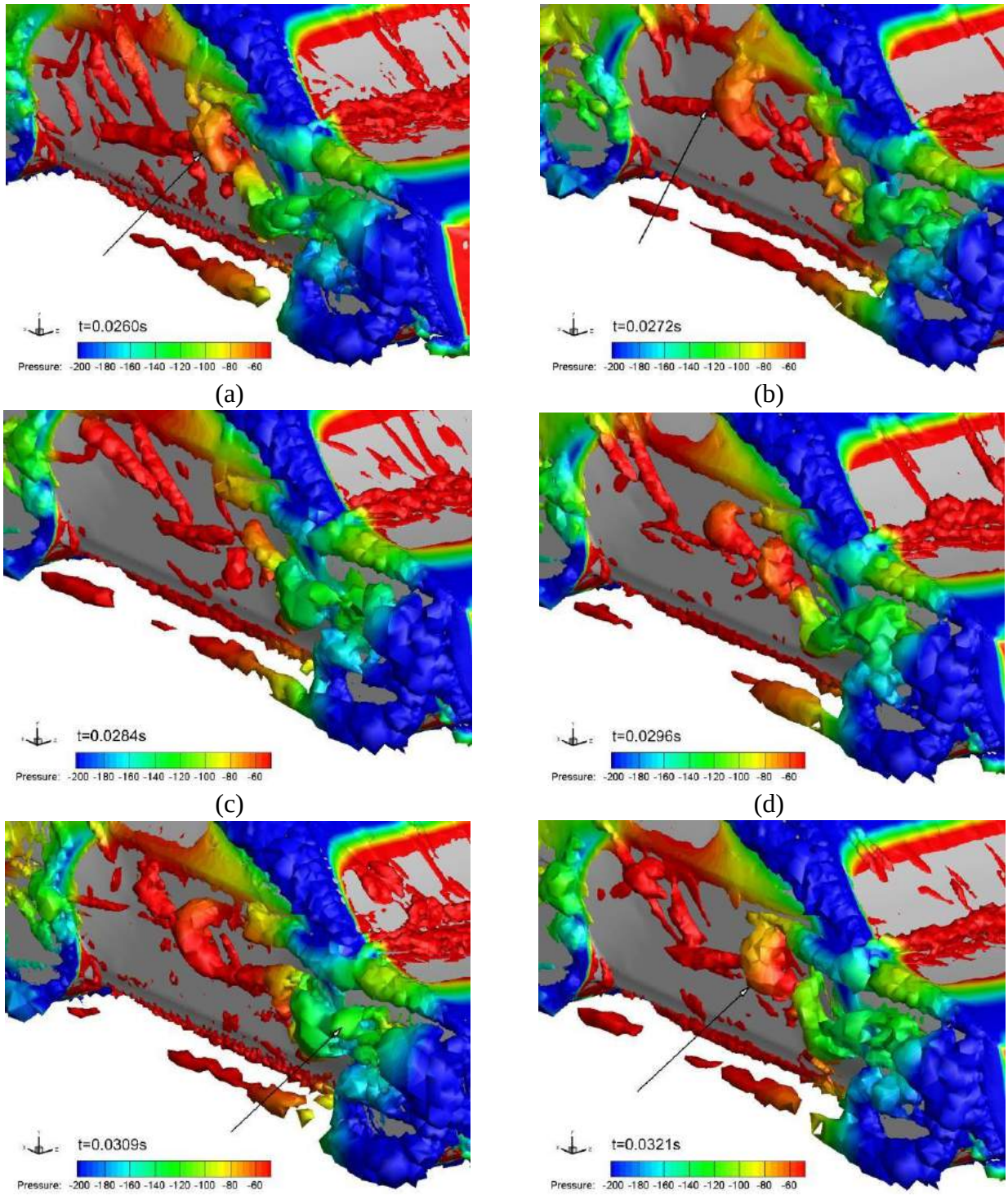

Figure 4.9 Helical right side vortex (vortex 4), shown by isosurfaces of Q-criterion $= \boldsymbol{3e5}$. The vortex started forming at the edge of the front bumper and had a slightly varying frequency (163, shown in (a) to (f), to 179 Hz) from one cycle to the next.

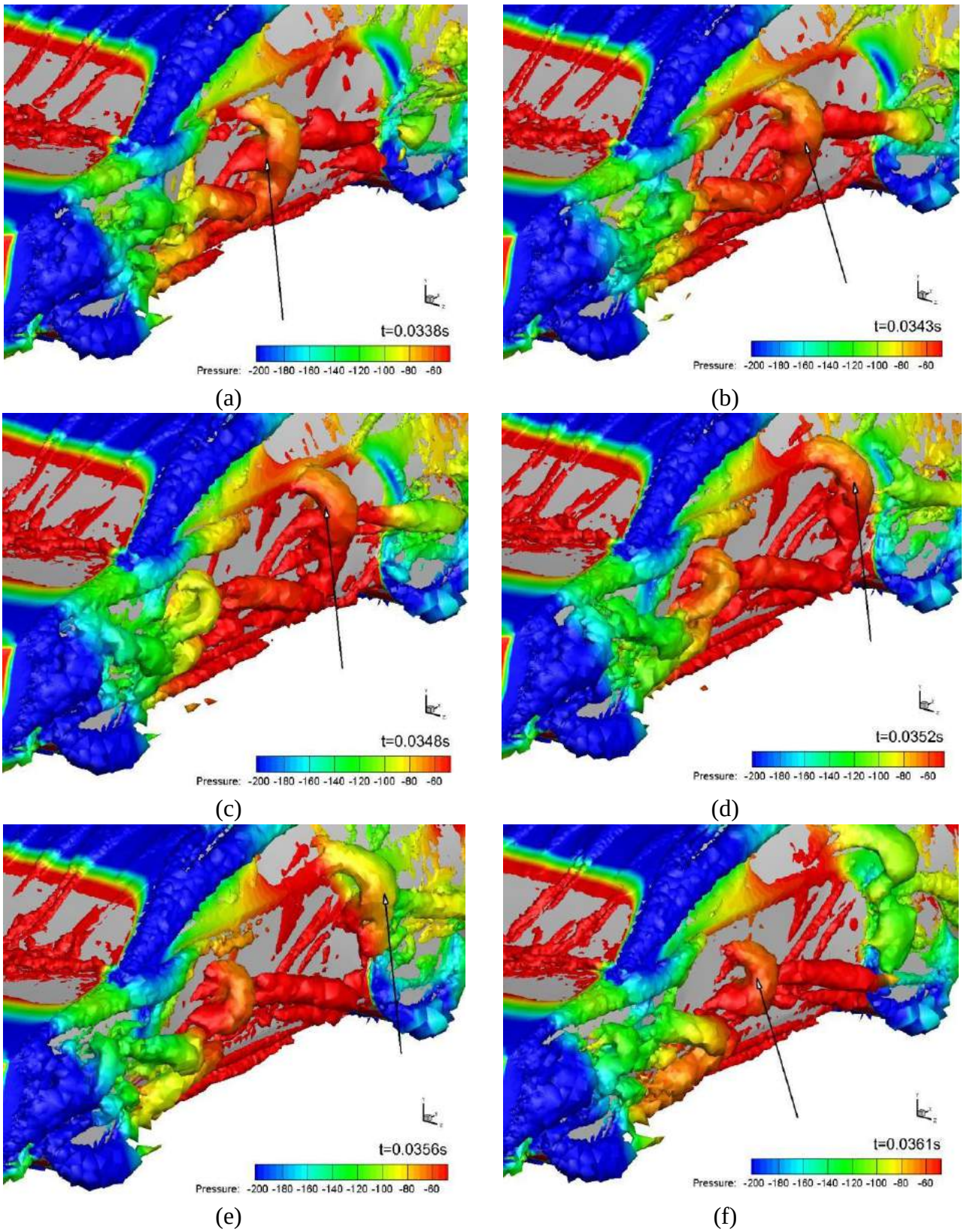

Figure 4.10 Helical left-side vortex (vortex 4)

4.1.2.2. During Interaction between the Two Vehicles

The interaction between the two cars started at t = 0.04s before they met each other, when the distance between them was ~2 car lengths, and continued after crossing until the cars were separated again by at least another two car lengths. This long interaction duration was evident in the fluctuation of the drag force (fig. 4.11) and side force coefficients for both cars (fig. 4.12) before they returned to the pre-interaction average values.

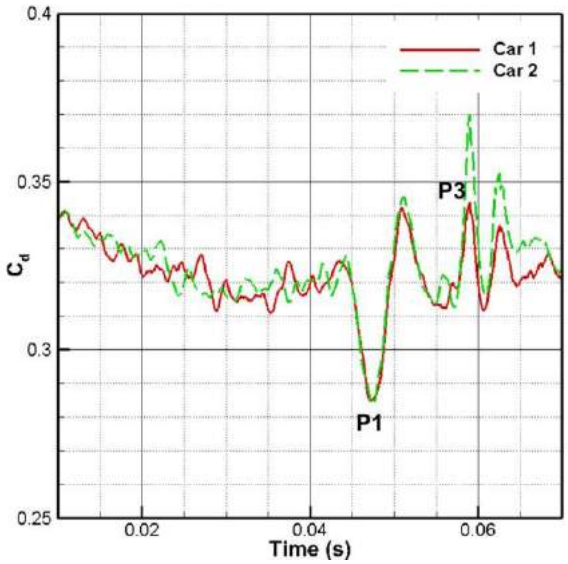

Figure 4.11 Drag coefficient time history

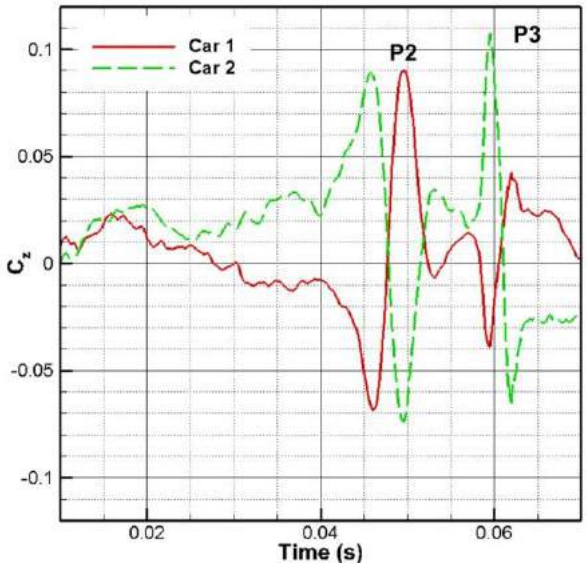

Figure 4.12 Side force coefficient time history

One noticeable observation was the alternation of these force fluctuations from one set of force coefficients to the other. For example, at t = 0.0475s (P1), the drag coefficient of both cars decreased to its minimum value (almost 20 percent less than average), while the side-force coefficient was at its average value, on the way to climbing up to its maximum value at t = 0.0495s (P2). At the same time, t = 0.0495s, the drag coefficient, was at its average value (0.32). At t = 0.0505s, the two cars were aligned side by side, front to rear. As the cars passed each other, another peak for both drag and side force coefficients was observed at t = 0.0595s (P3). The pressure distribution on the sides of each car during the crossing contributed to the fluctuations in the side-force coefficient. At the maximum side force value (P2), the low-pressure region between the two cars reached its maximum extent and strength (fig. 4.13). This low pressure region grew as the two cars approached each other, pulling the two cars toward each other and contributing to the fluctuations in side force (fig. 4.14). The main vortical structures around the two vehicles did not change in shape or direction during the interaction, but they lost their periodicity (fig. 4.15).

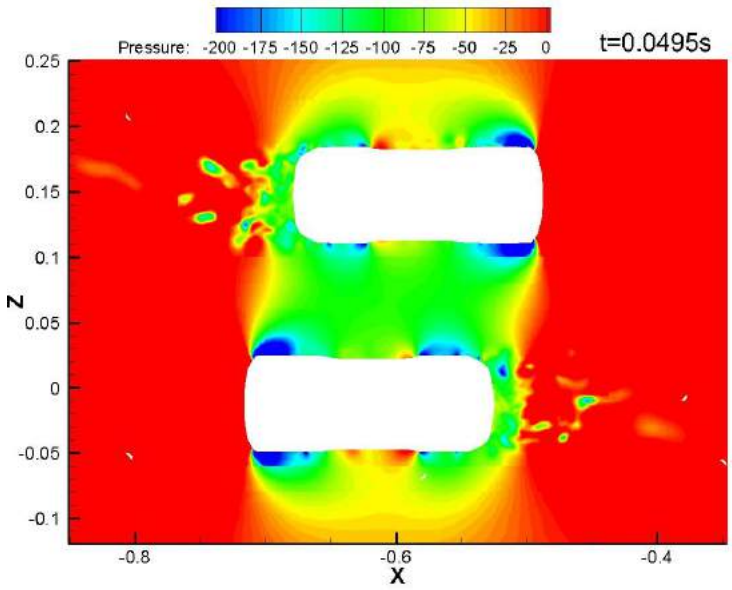

Figure 4.13 Horizontal slice at y=0.02 showing the pressure distribution around the cars at maximum side force (P2 in figure 4.12)

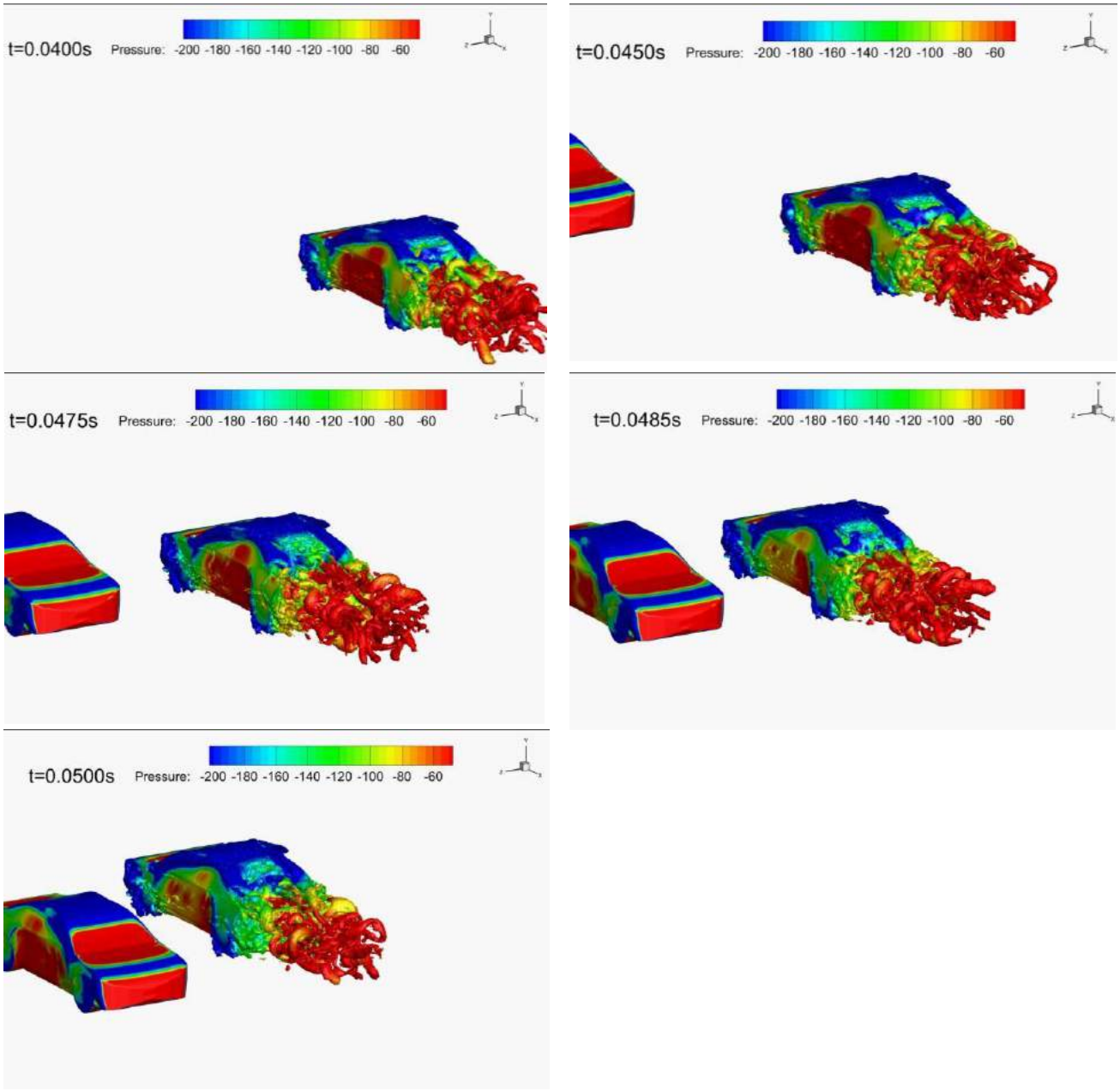

Figure 4.14 Overall flow pattern and pressure distribution on car sides during interaction

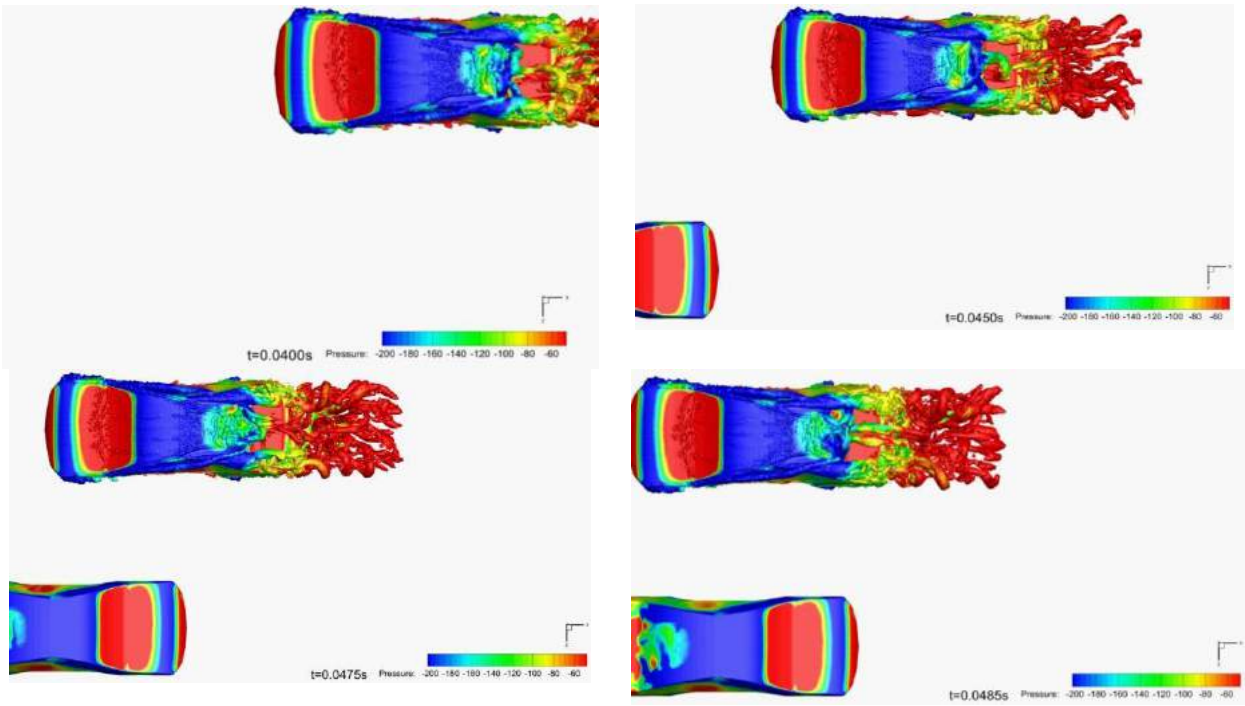

Figure 4.15 Top view of vortical structures during interaction

The lift coefficient (fig. 4.16) hovered close to zero for both cars and did not show significant variation during interaction in comparison to its average fluctuation frequency.

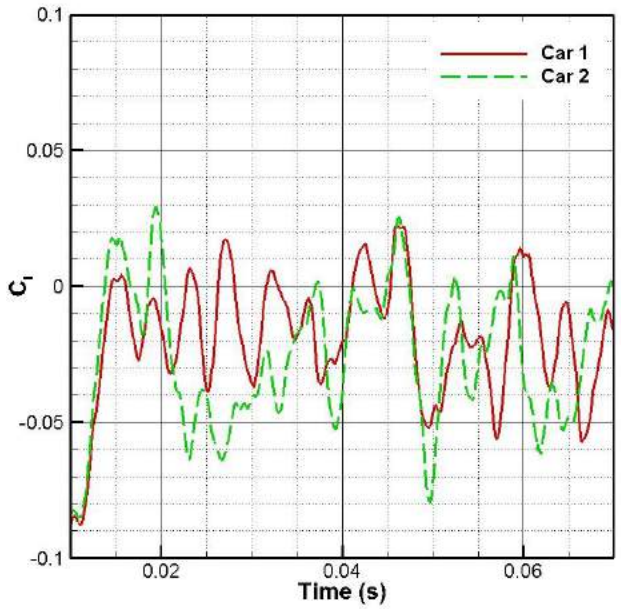

Figure 4.16 Lift coefficient time history

The roll coefficient for both cars (fig. 4.17) was small, which was expected, as the car geometry was symmetrical around the vertical plane passing through its centerline; consequently, the streamwise vortical structures were symmetrical around that same plane. The vortices were oriented along the longitudinal axis, not the vertical axis; there were little variation between the vertical forces acting on each side of the car to cause a significant roll moment. Still, within that small magnitude of roll moment (less than 0.0075 for either car), the interaction caused a spike at t=0.0495s before returning to normal.

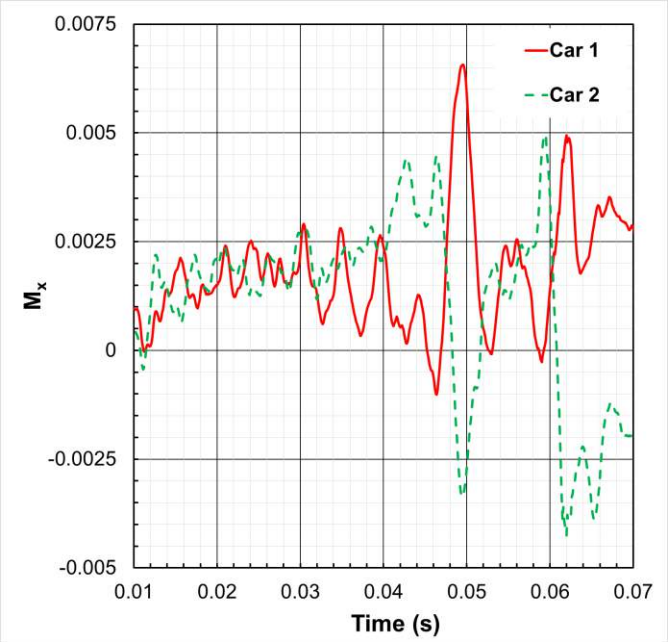

Figure 4.17 Roll moment coefficient time history

The yaw moment coefficient (fig. 4.18) did not show a periodic pattern before the interaction started, varying between 0 and 0.075 for either car; that can be attributed to the large number of symmetrical, streamwise vortical structures of varying shedding frequencies on each side of the car, with no particular vortex having a dominant effect over the others. Again, there was a small spike at t=0.0460s, but this peak was at the same order of magnitude of the largest fluctuation of the coefficient before the interaction started. There was no effect on the pitch moment coefficient (fig. 4.19).

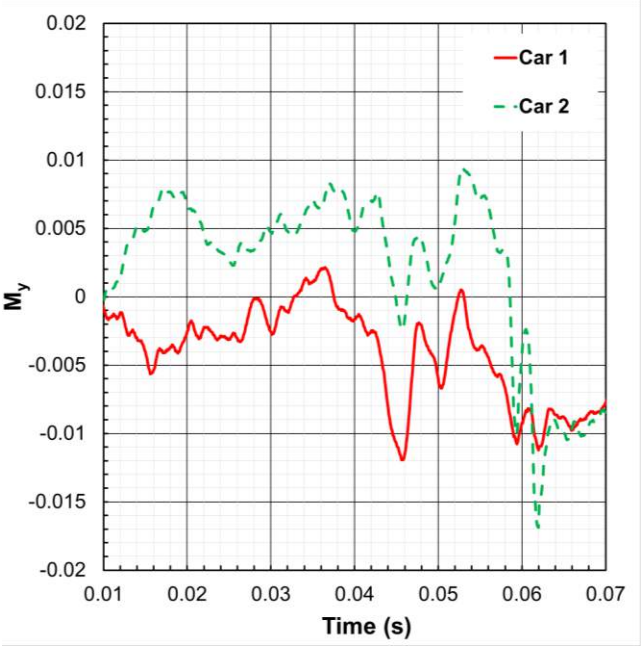

Figure 4.18 Yaw moment coefficient time history

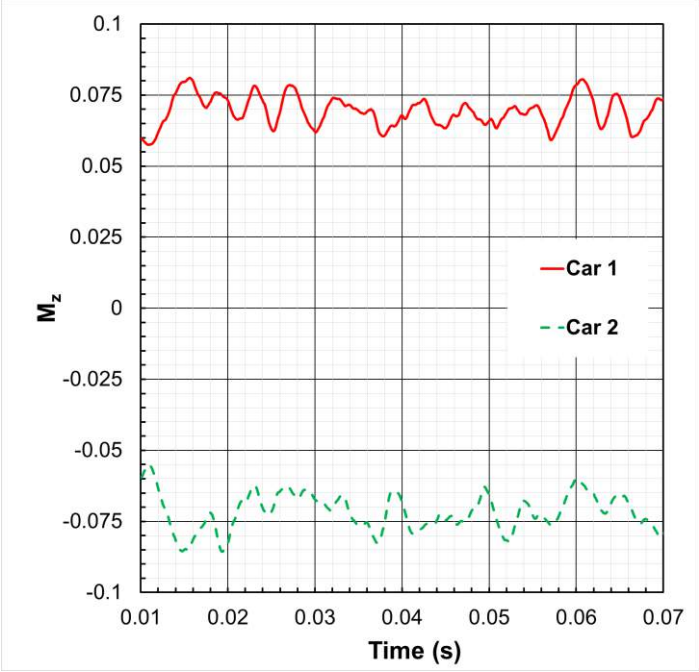

Figure 4.19 Pitch moment coefficient time history

4.1.3 Car Overtaking a Truck

4.1.3.1. Before Interaction between the Two Vehicles Started

The mean drag coefficient (fig. 4.20) of the car in this scenario (0.28) was slightly lower than the scenario involving two cars crossing each other (0.32). This was likely due to the longer pre-interaction simulation time of the overtaking case, facilitating the stabilization of forces and moments acting on both vehicles. The longer simulation time was made possible by the low relative velocity between the car and truck (6 m/s) in comparison to the relative velocity between two cars moving in opposite directions (60 m/s). Spectral analysis of the pre-interaction drag coefficient showed three peaks at 45 Hz, 50 Hz, and 55 Hz that were not observed in the two-car-case (the smaller time interval sample in that case was likely a factor again), as well as a peak at 95 Hz, which broadly corresponded to the 100-Hz peak observed in the previous case. Another possible reason for this lower drag coefficient value was the presence of the car in the downstream "shadow" of the truck. The drag coefficient of the truck before interaction was 0.68, within the expected range of 0.6-0.9 for this type of vehicle.

The lift coefficient of the car was ~0 (fig. 4.21), in good agreement with the two-car-case. It oscillated around this value because of the different shedding frequencies of vortices on the top and bottom of the car. The truck, however, oscillated around a negative lift coefficient value (-0.3). This was likely due to the dominant effect of the low pressure region beneath the long trailer, creating a force that pushed the truck downward. The average side force coefficient of the car was 0.05, and that of the truck was ~0.

The side force coefficient for the truck was ~0 but about 0.05 for the car (fig. 4.22). The non-zero side force for the car was likely caused by the fact that the car was in the wake of the truck, where the flow was not strictly parallel to the car axis.

The yaw moment coefficient of the car (fig. 4.23) oscillated irregularly around a low mean value of 0.01, while that of the truck irregularly oscillated around 0. The average roll moment coefficient (fig. 4.24) of both vehicles was ~0.

4.1.2.2. During Interaction between the Two Vehicles

The interaction between the two vehicles started at 0.7s into the simulation, when the car was 5.2 car lengths behind the truck. The car's drag coefficient climbed up gradually, until the rear of the car was aligned with the rear of the truck, at which point the drag coefficient rapidly rose and reached 0.54, a 100 percent increase on the pre-interaction mean value. At this point in the simulation, the front ends of the car and the truck were aligned side by side. The side force coefficient (fig. 4.22) of the car also increased by ~900 percent at 0.95s. The lift coefficient dropped slightly to -0.16, which was within the range of the pre-interaction oscillation. The car started exiting the high-pressure region in front of the truck, and all force coefficient rapidly dropped back to their pre-interaction average values. There was a distinct jump in the yaw moment coefficient to 0.07 from a pre-interaction average of ~0.01, and a smaller jump of the rolling moment coefficient from 0 to 0.026, which matched the maximum value of the pre-interaction oscillation.

The truck was relatively unaffected by the passing maneuver, with all force and moment coefficients showing no appreciable change. This was expected given the size difference between the two vehicles. The pitch moment coefficient of both vehicles (fig. 4.25) showed no oscillations during the interaction.

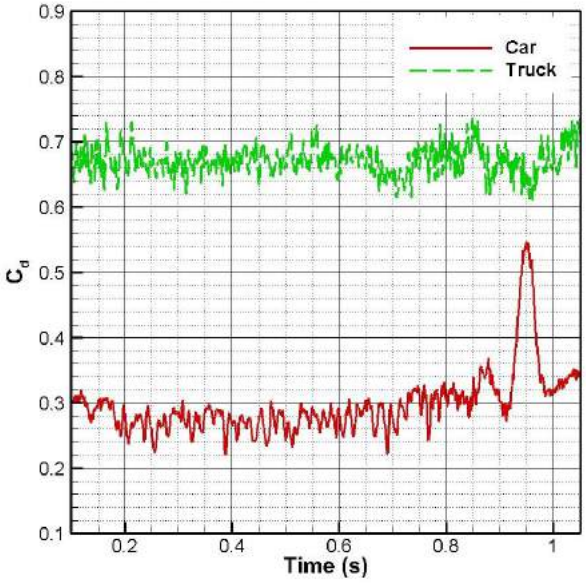

(a)

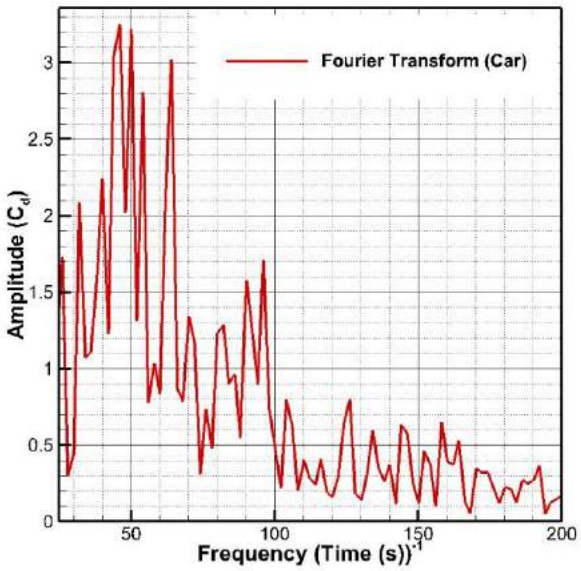

(b)

Figure 4.20 (a) Drag coefficient time history, and (b) FFT analysis of car drag coefficient before vehicle interaction (b)

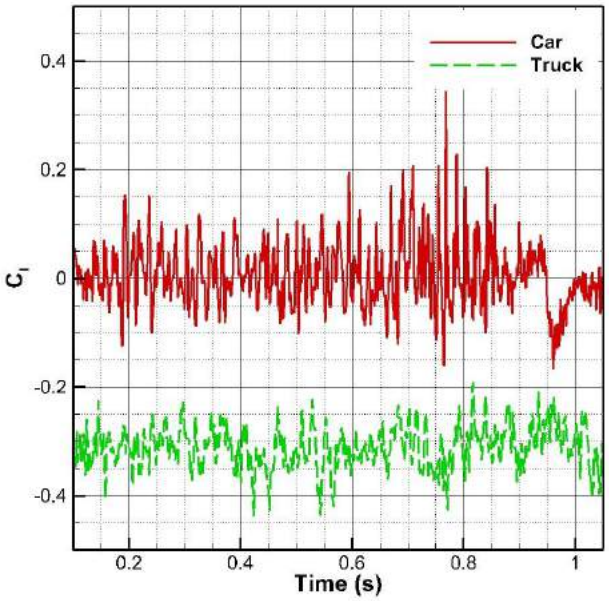

Figure 4.21 Lift coefficient time history

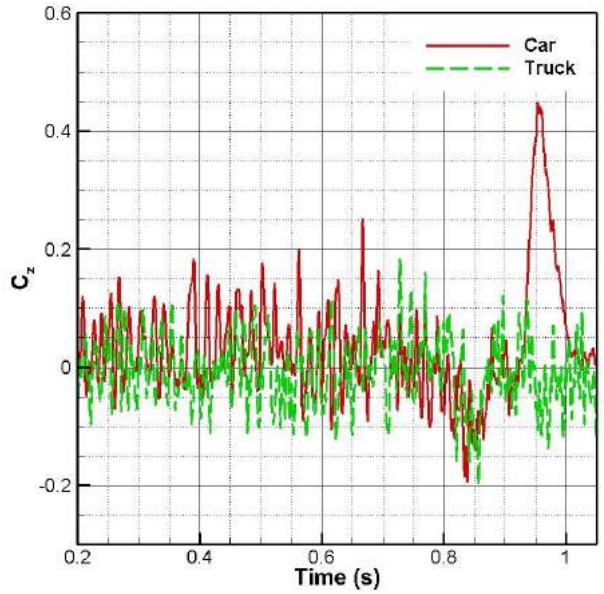

Figure 4.22 Side force coefficient time history

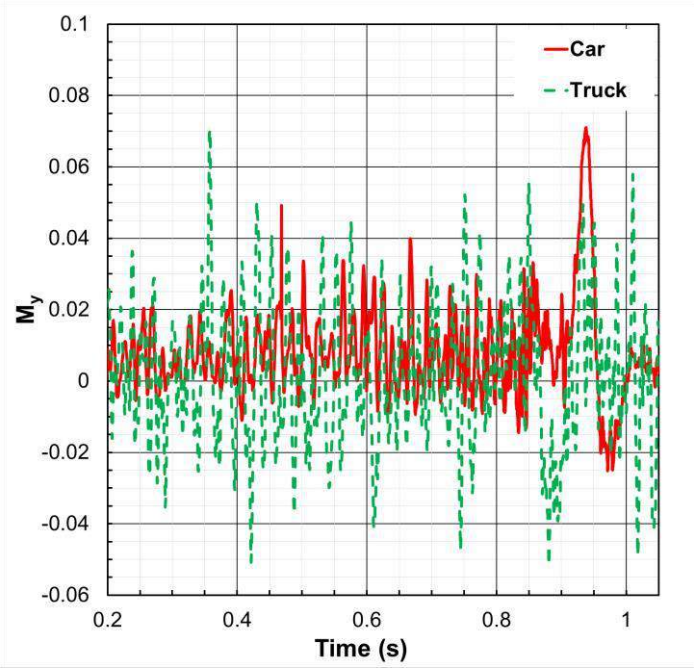

Figure 4.23 Yaw moment coefficient time history

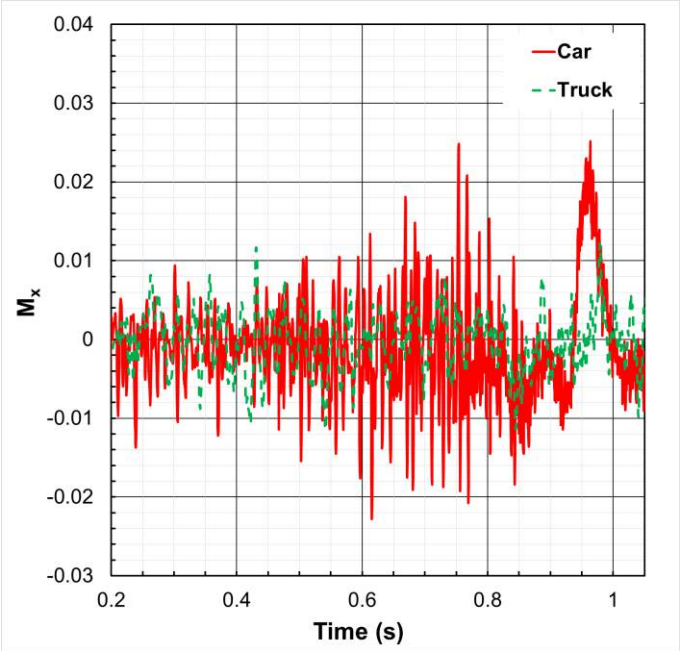

Figure 4.24 Roll moment coefficient time history

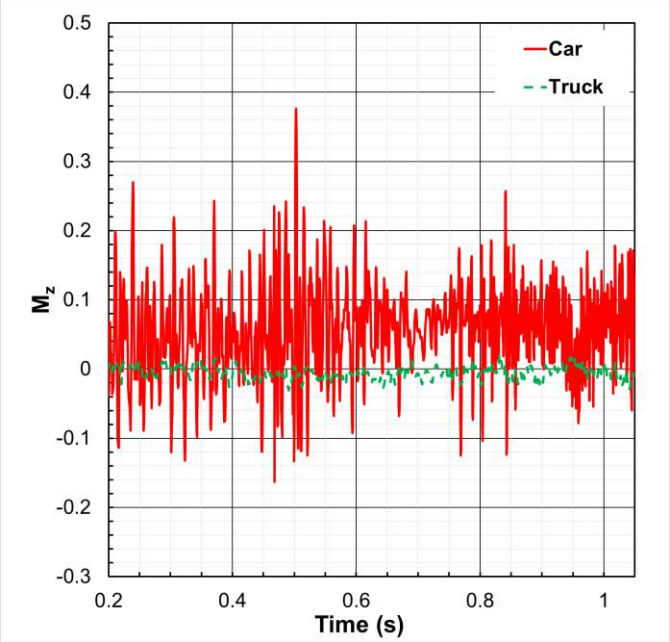

Figure 4.25 Pitch moment coefficient time history

4.1.4 Car-Truck Crossing

4.1.4.1 Before Interaction between the Two Vehicles Started

The average car drag coefficient was 0.31 (fig. 4.26), in good agreement with the first case (two cars crossing each other). The average lift coefficient was ~-0.3 (fig. 4.27), and the average side force coefficient was ~0 (fig. 4.28). The truck's drag coefficient during the stable portion of the flow around it (between 0.05s-0.07s in the simulation) was 0.69 in comparison to 0.68 in the previous case. The car's average side force coefficient was ~0, while its average lift coefficient was -0.03. Similar to the previous case, the flow around the truck was producing a negative vertical force on the truck's surface, with its average lift coefficient being -0.3. The truck's side force coefficient oscillated with a higher amplitude than the car, but the average value was approximately zero. The vortical structures surrounding the truck before interaction

were dominated by the rear vortex shed off the top edge of the trailer box (fig. 4.29 through fig. 4.31).

4.1.4.2 During Interaction between the Two Vehicles

The interaction between the car and the truck started when they were separated by six car lengths, at 0.07s during the simulation. All force and moment coefficients, for both vehicles, showed a similar pattern: a rapid change to a positive or negative peak value, followed by a swing to another peak value with an opposite sign. The car's drag coefficient rose from 0.31 to 0.37 as the two vehicles started getting closer to each other, before quickly dropping to 0.11 (P1) and rebounding to 0.41 (P2) during the vehicle crossing. The side force coefficient rose from ~0 to 0.45 (P3), then dropped to -0.35 (P4) during the same time period. The yaw moment coefficient of the car only showed one peak, changing from ~0 to -0.05, and the effects on the yaw moment continued to the end of the simulation (fig. 4.32). The roll moment coefficient changed to 0.019, then dropped to -0.017 (fig. 4.33).

The truck's drag coefficient rose to 0.74, then slowly dropped to 0.6 by the time the front ends of both vehicles were side by side. The crossing between the two vehicles did not cause a change in the truck's lift coefficient. Its side force coefficient dropped to -0.15 before rising to 0.15. This range of change was close to the oscillation maximum/ minimum amplitudes of the pre-interaction period (0.12 and -0.07, respectively). The pitch moment coefficient for both vehicles (fig. 4.34), as in all simulation cases, was of weak importance because of the low likelihood of vehicle instability around this axis (i.e., a vehicle will not typically tip over its front or back end because of the long longitudinal distance between its center of gravity and each of the front or rear wheels).

The moments acting on the truck were weakly affected by the crossing, with both the yaw and rolling moment coefficients changing values within the range of their pre-interaction values.

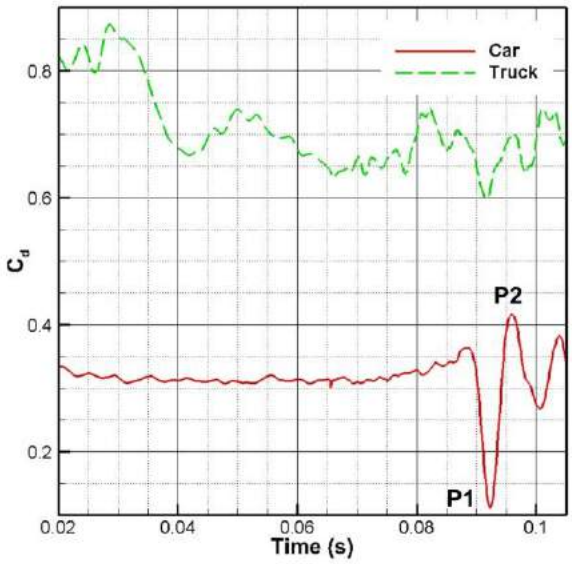

(a)

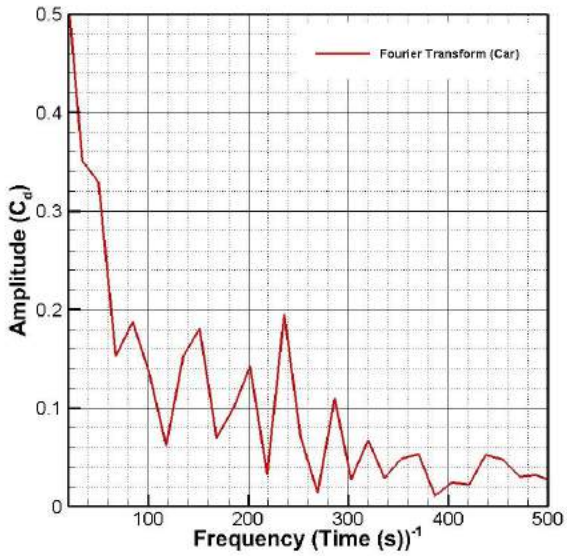

(b)

Figure 4.26 (a) Drag coefficient time history, and (b) FFT analysis of car drag coefficient before vehicle interaction

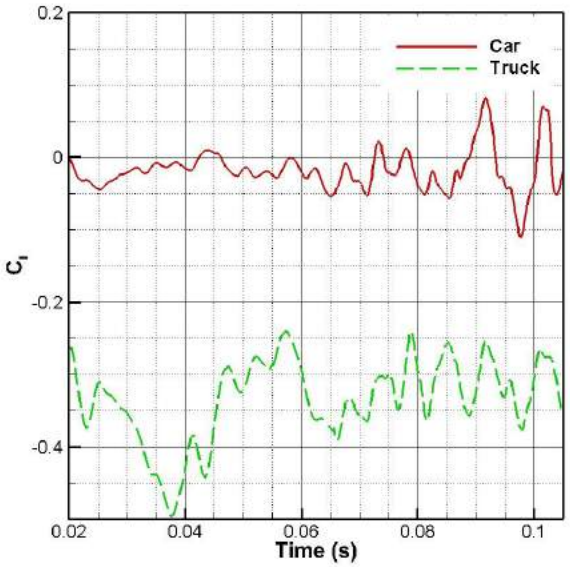

Figure 4.27 Lift coefficient time history

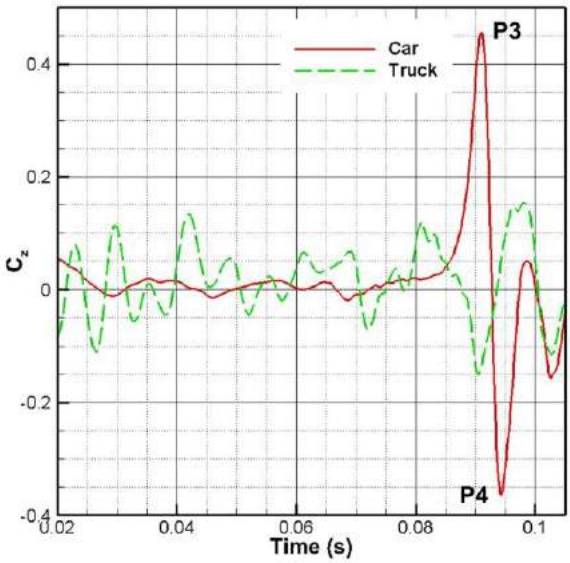

Figure 4.28 Side force coefficient time history

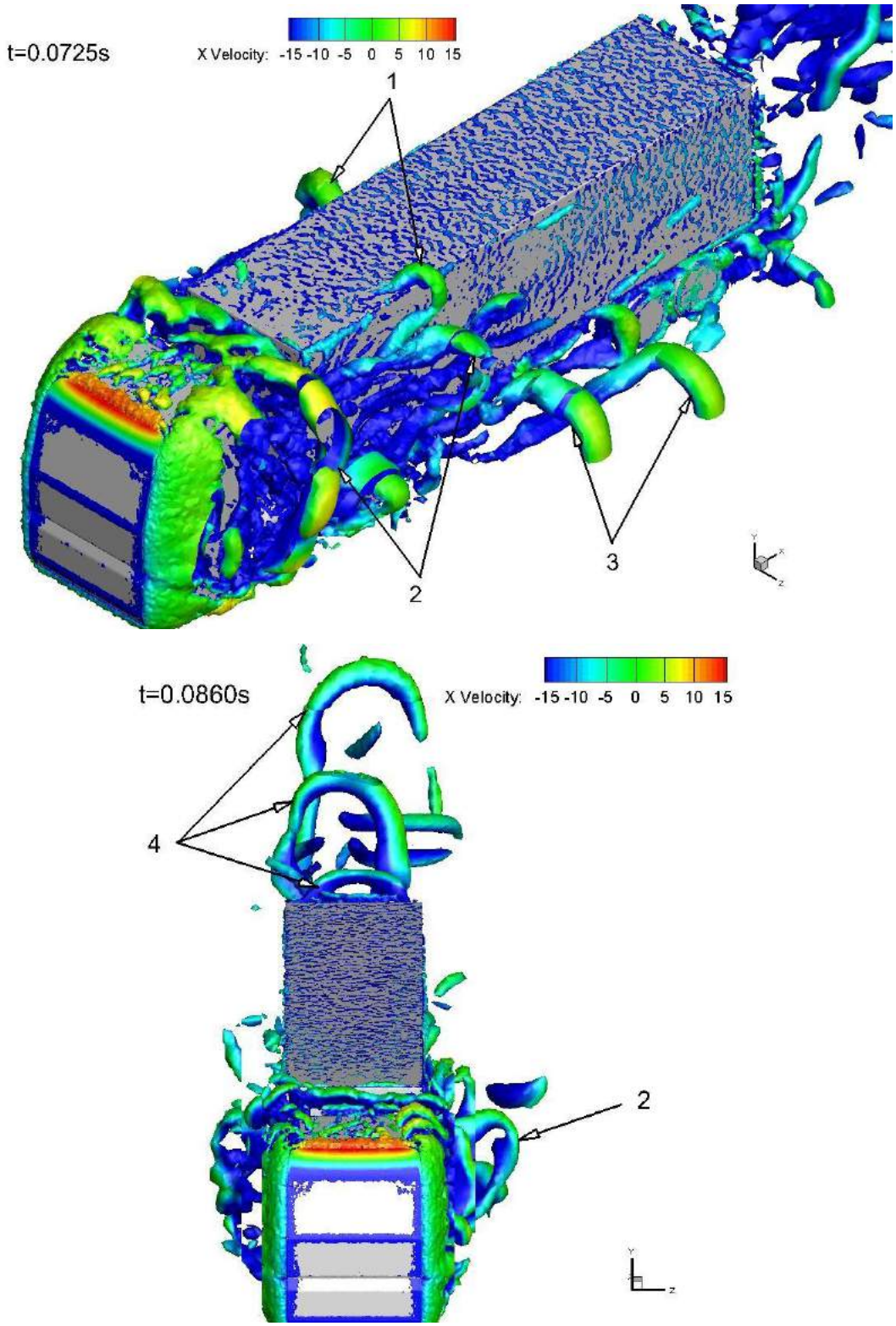

Figure 4.29 Defining vortical structures using isosurfaces of the Q-criterion

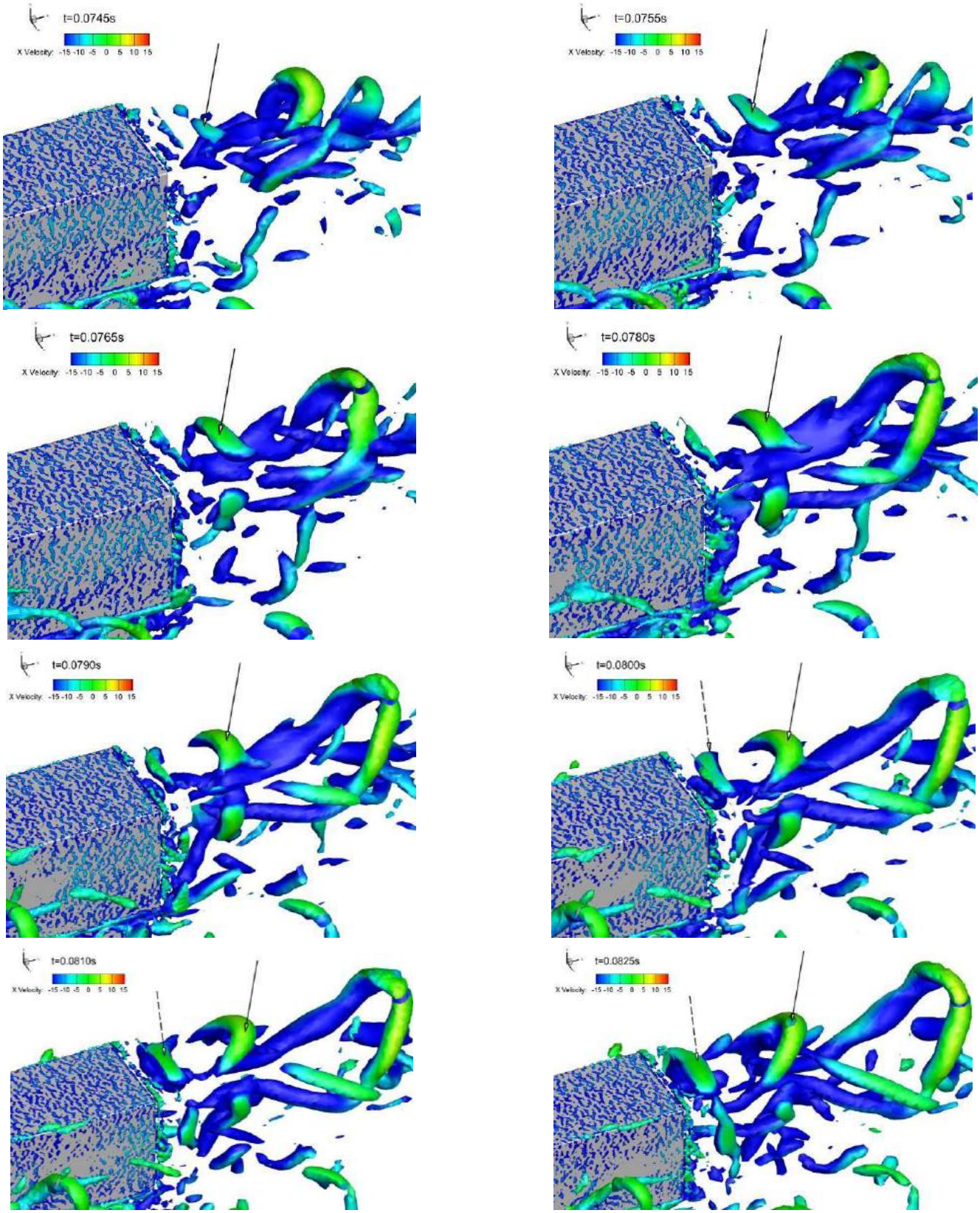

Figure 4.30 Rear vortex, showing isosurfaces of Q-criterion = $\boldsymbol{4e5}$.

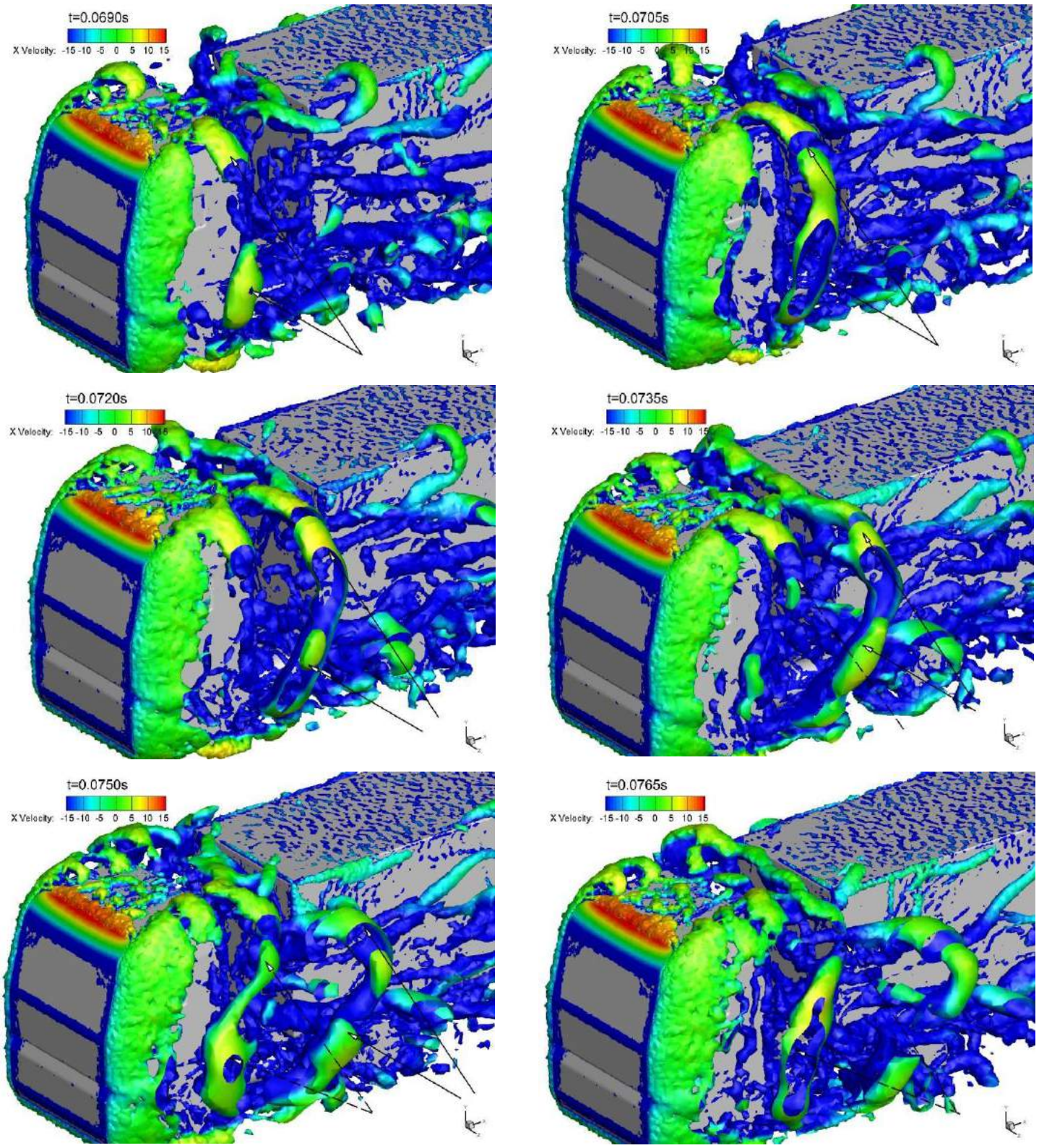

Figure 4.31 Side vortex, showing isosurfaces of Q-criterion = $\boldsymbol{3e5}$.

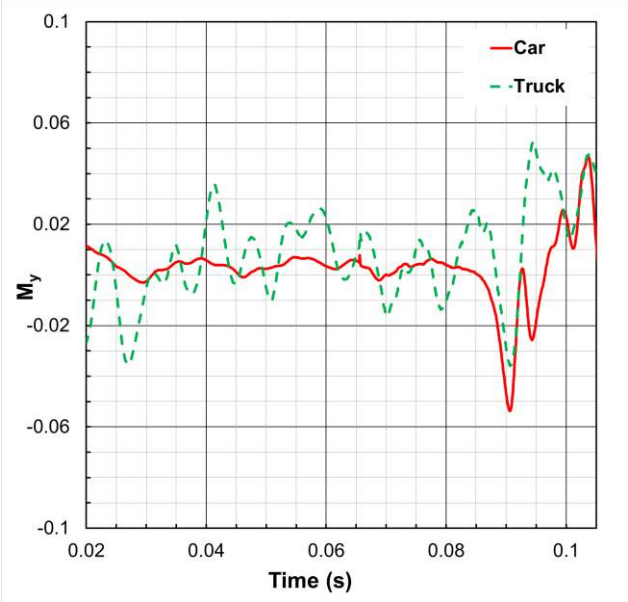

Figure 4.32 Yaw moment coefficient time history

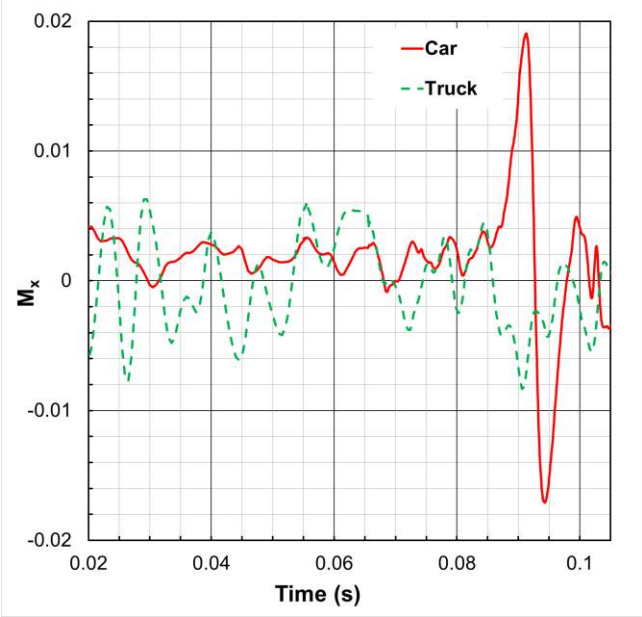

Figure 4.33 Roll moment coefficient time history

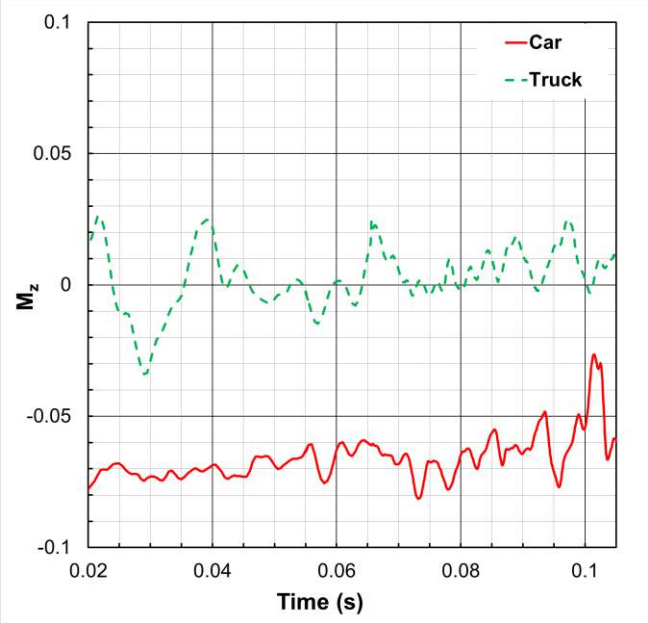

Figure 4.34 Pitch moment coefficient time history

4.2. Vehicle Interaction Scenarios in the Presence of 30° Crosswinds

4.2.1 Experimental Validation of the Simulation Results

Wind tunnel experimental measurements of the drag force acting on a single car angled at 30° to the incoming airflow were conducted. The force balance was parallel to the airflow. The drag force along the longitudinal axis of the car was calculated by recording the drag and side forces acting on the vehicle during each experimental run, then evaluating the sum of the components of these forces along the longitudinal axis of the car, angled at 30° to the force balance.

The average C_d value obtained from the experimental results was 0.34 (fig. 4.35), 15 percent lower than the simulation results. The higher results obtained from the simulations was likely due to the separating distance between the two vehicles not being long enough to allow for the flow to reach a quasi-stable state.

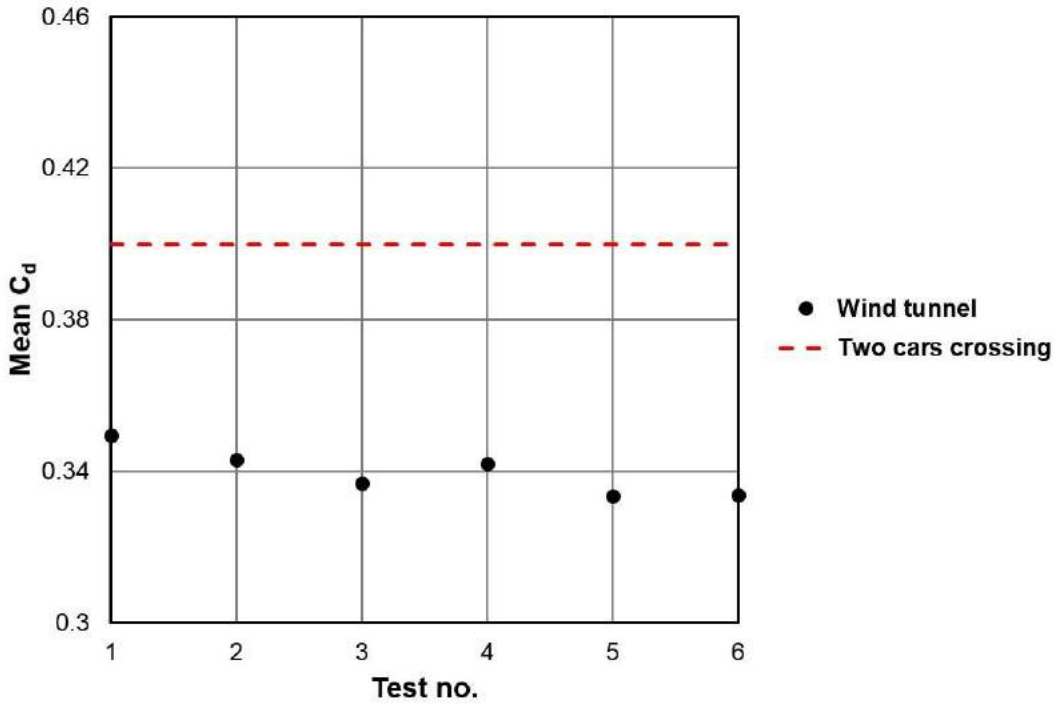

Figure 4.35 Experimental validation of single car drag coefficient in the presence of crosswinds

4.2.2 Two Cars Crossing with Crosswinds at a 30^o Angle

4.2.2.1 Before Interaction between the Two Vehicles Started

The mean drag coefficient of both cars before the crossing was 0.40, a 34 percent increase over the same car's drag coefficient without the presence of crosswinds (fig. 4.36). The car was less streamlined when the airflow was affecting it at an angle, and an increase in drag force was expected. The lift coefficient showed two phases, the first with a mean value of 0.14 (0.15s to 0.03s in the simulation), and a second phase with a mean value of -0.10 (0.03s to 0.04s in the simulation) (fige 4.37). The side force coefficient stabilized later than the other two force coefficients. The mean value for both cars was 1.47. This was an indication of the stronger side forces acting on the vehicles by the crosswinds (fig. 4.38) in comparison to the side forces experienced in the similar case without crosswinds.

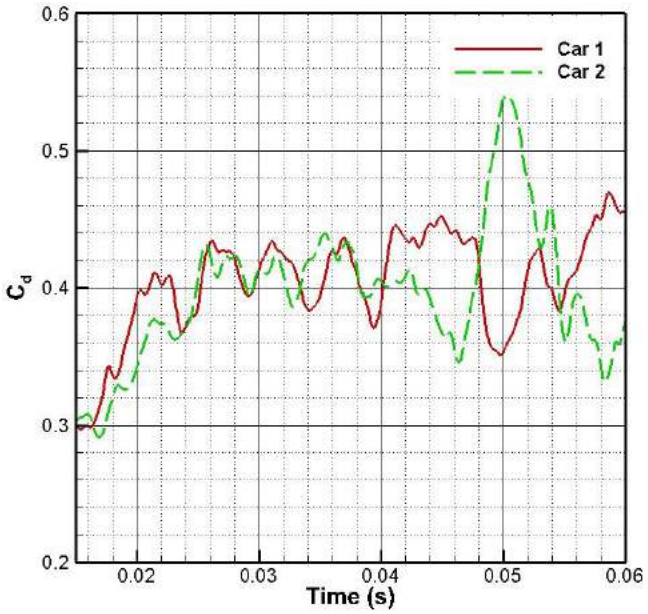

Figure 4.36 Drag coefficient time history

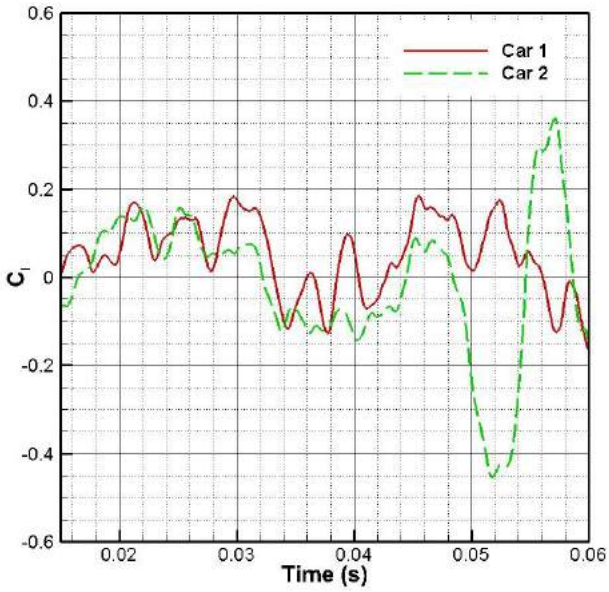

Figure 4.37 Lift coefficient time history

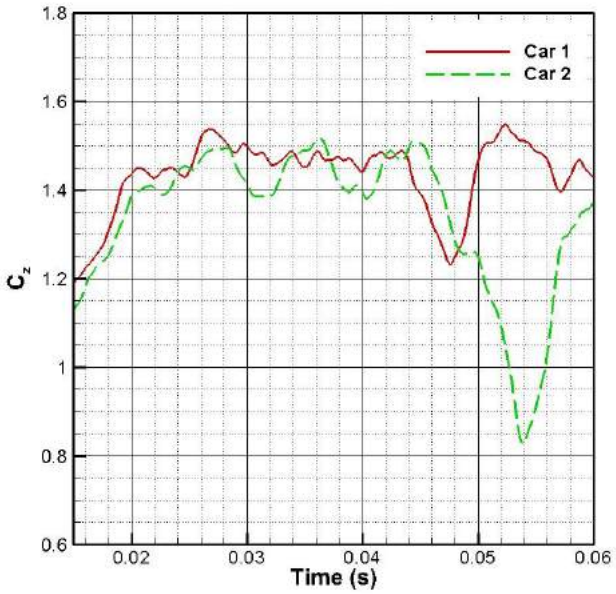

Figure 4.38 Side force coefficient time history

4.2.2.2 During Interaction between the Two Vehicles

As the vehicles approached each other, one car experienced a jump in its drag coefficient to 0.54 (Car 2) (fig. 4.36), while the other was momentarily shielded from the effects of the crosswind, and the drag forces acting on it dropped by 15 percent in comparison to the pre-interaction mean value. The windward car (Car 2) also experienced the largest deviation of side forces. Its side force coefficient changed from a mean value of ~1.47 to 0.84 (fig. 4.38). The side force coefficient of the car on the leeward side dropped to 1.23. This pattern was repeated with the lift coefficient: the windward car's coefficient changed to -0.45, with no appreciable change for the leeward car.

The yaw moment coefficients (fig. 4.39) showed the same trend as the force coefficients: the windward car showed a greater deviation from average (-0.17 to -0.10) than the leeward car (0.20 to 0.18). Both roll and pitch moment coefficients show no appreciable change from the pre-interaction average (fig. 4.40 and fig. 4.41).

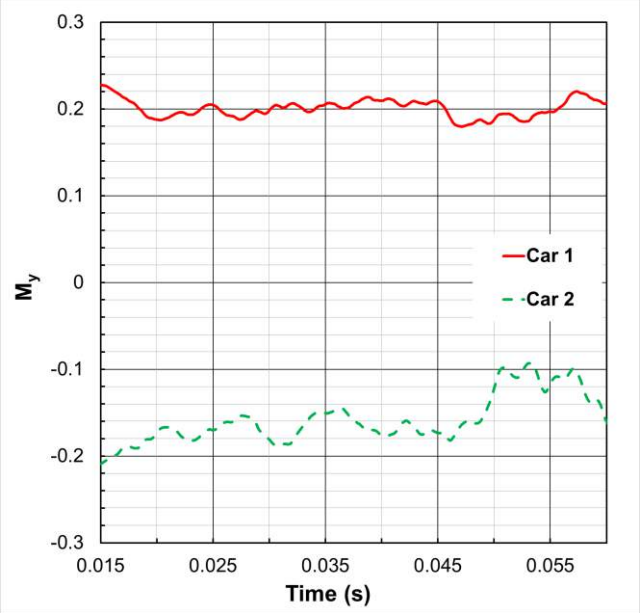

Figure 4.39 Yaw moment coefficient time history

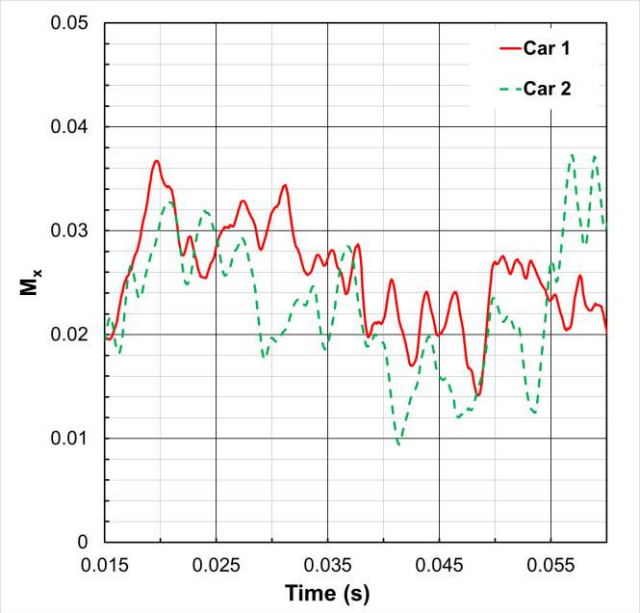

Figure 4.40 Roll moment coefficient time history

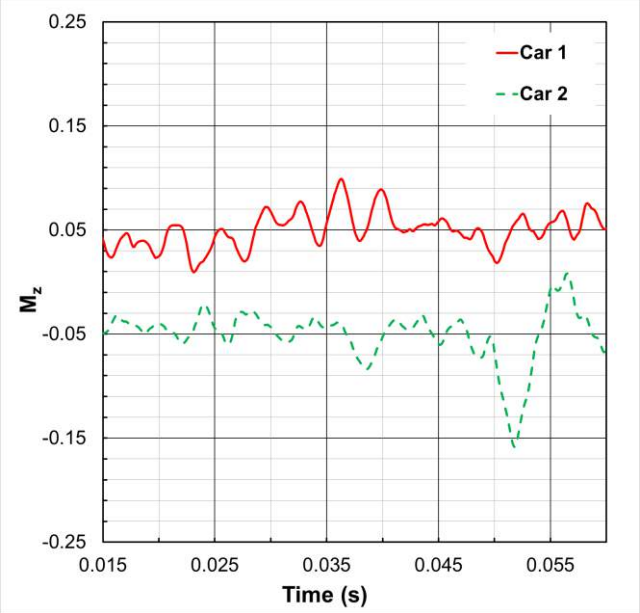

Figure 4.41 Pitch moment coefficient time history

4.2.3 Car-Truck Crossing with Crosswinds at a 30^o Angle

4.2.3.1 Before Interaction between the Two Vehicles Started

The car's mean drag coefficient was 0.4 (fig. 4.42). This was lower than the 0.55 value reported in the previous case with crosswinds, likely because of the longer duration of the simulation before interaction started. The car's mean lift coefficient was -0.14, while its mean side force coefficient as 1.38 (fig. 4.43 and fig. 4.44).

The truck had a higher mean drag coefficient when crosswinds were present (1.4) than without crosswinds (0.68-0.70), and it no longer had a downward vertical force acting on it. Its mean lift coefficient was 0.41, while its mean side force coefficient (3.3) was also significantly higher than the cases without crosswinds.

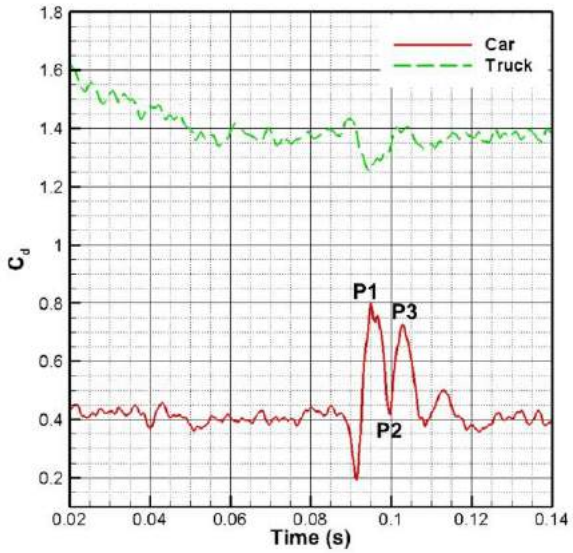

Figure 4.42 Drag coefficient time history

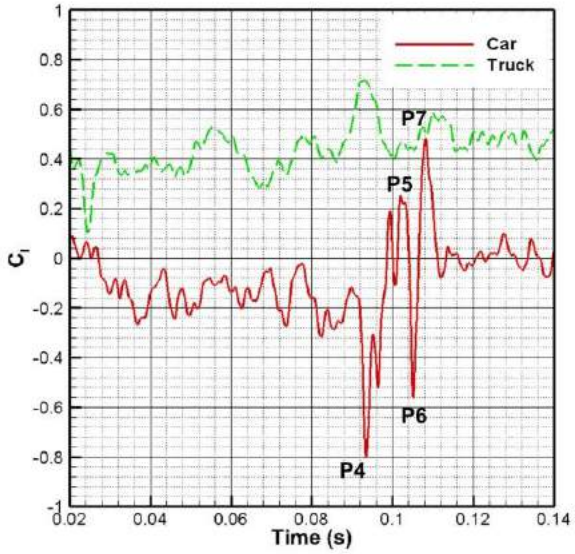

Figure 4.43 Lift coefficient time history

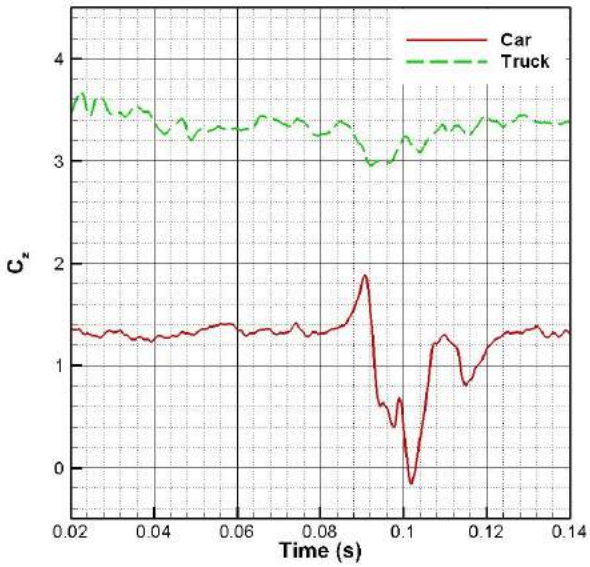

Figure 4.44 Side force coefficient time history

4.2.3.2 During Interaction between the Two Vehicles

The interaction started at 0.08 and ended at 0.12s. The car's drag coefficient abruptly dropped by 50 percent when it approached the truck, then increased by 100 percent of the mean value to 0.8 (fig. 4.42, P1). As the car passed the tractor unit, it dropped again to 0.45 (P2) then rose to a peak of 0.72 (P3) at 0.104s. The side force coefficient of the car rose briefly from 1.3 pre-interaction to 1.9, then dropped quickly to -0.2, before increasing to 1.3 (fig. 4.44). After a slight dip to 0.8 at 0.175s, the side force coefficient returned to the pre-interaction mean value. The lift coefficient (figure 4.43) of the car fell to -0.8 at 0.074s (P4), then showed a rising trend to a peak of 0.24 (P5). This is followed by a fall to -0.56 (P6), and a subsequent rise to a maximum value of 0.48 (P7), and finally it settled to a mean value of ~0. The yaw moment coefficient of the car switched from a negative value pre-interaction (-0.19) to a positive peak value (0.07) during the vehicle crossing, indicating a switch in the yaw moment direction (fig. 4.45). It returned to a mean value of -0.19 toward the end of the interaction.

The truck was weakly affected by the crossing, with its drag coefficient dropping by 10 percent to 1.25 before rebounding to its pre-interaction average (fig. 4.42). Its lift coefficient rose to 0.7 at 0.093s, then fell back to a value (0.48) close to its pre-interaction mean. The truck's side force coefficient gently dropped to 3.0 early in the interaction, a 10 percent decrease, then returned to its pre-interaction mean value (fig. 4.44). The truck's moment coefficients were not strongly affected during its interaction with the car.

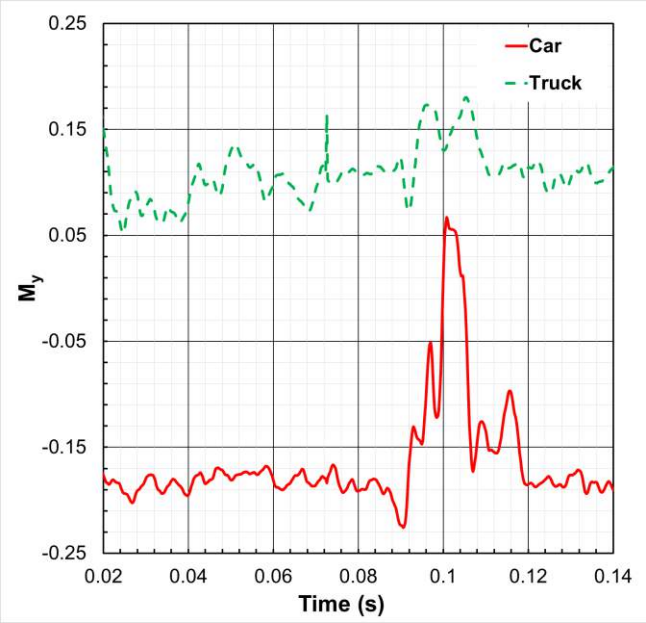

Figure 4.45 Yaw moment coefficient time history

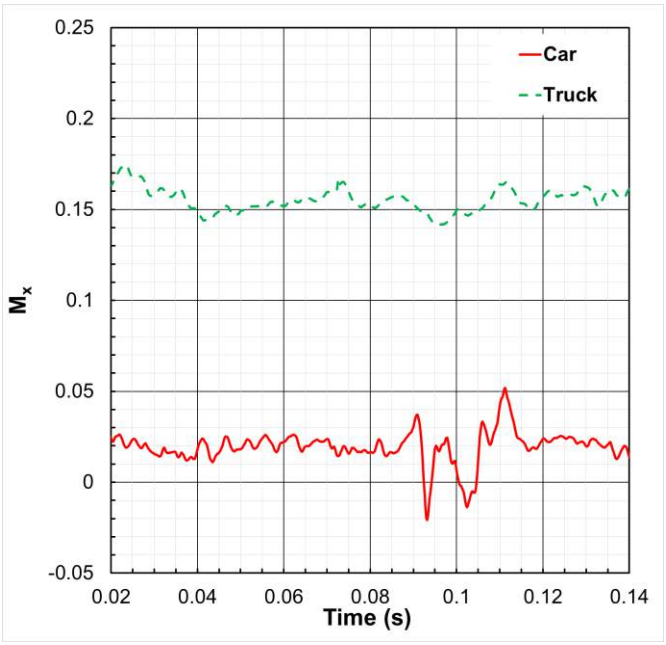

Figure 4.46 Roll moment coefficient time history

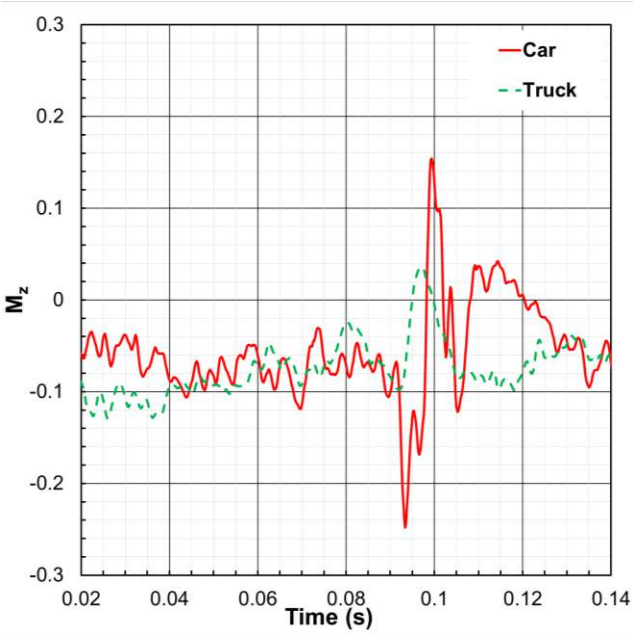

Figure 4.47 Pitch moment coefficient time history

Chapter 5 Conclusions and Recommendations

This study conducted high-fidelity CFD simulations for two vehicles (car and truck) crossing or overtaking each other with and without crosswinds. The simulations were first validated by using wind tunnel measurements for a single car at 0- and 30-degree yaw angles and a single truck at a 0-degree yaw angle. The main conclusions that affect vehicle safety for different cases are summarized below.

5.1 Case 1: Two Cars Crossing

During interaction, the most significant effect of one car on the other was on the side force and yaw moment. Under the conditions analyzed, these effects lasted for ~0.02s, and no fluctuation lasted more than 0.005s, so the impulse of any change in side force was small. The two cars affected each other similarly, and the interaction did not change the vortical structures surrounding each car.

5.2 Case 2: Car Overtaking a Truck

The car was affected by the truck's wake for a longer duration of time than in Case 1 (0.3s), and the magnitudes of the change in forces and moments were also much larger. These forces and moments showed less change in the initial phase of the interaction. The fluctuations reached their peak when the car passed the truck's front end, showing the role of the shape of the front end of trucks in determining the magnitude of the forces acting on other vehicles sharing the road with them. It is worth noting that the relative overtaking speed of the car (12 mph) was at the higher end of the spectrum of typical overtaking speeds, so the aerodynamic effects were magnified and lasted shorter as well.

5.3 Case 3: Car-Truck Crossing

The larger size of the truck caused larger changes in the car's force and moment coefficients, and the interaction lasted for a longer duration (0.03s) than in Case 1. The side force acting on the car swung in direction from side to side during this duration, and although the fluctuations in side force reached amplitudes that were 500 percent larger than the maximum amplitude in Case 1, the period of this change in force was quite small (0.01s).

5.4 Case 4: Two Cars Crossing with Crosswinds at a 30^{o} Angle

The windward car experienced the largest change in forces and moments. The overall trend was similar to that in Case 1.

5.5 Case 5: Car-Truck Crossing with Crosswinds at a 30^{o} Angle

The presence of crosswinds changed the interaction pattern in comparison to the similar case without crosswinds (Case 2). There were more fluctuations as the car entered and exited the gap between the tractor unit and trailer of the truck. As in all cases, the truck was minimally affected during the crossing.

5.6 Future Work

To fully investigate the effects of crosswinds on vehicle interactions, more CFD simulations need to be run with incrementally larger crosswind angles. The effects of lateral separating distance between the vehicles can be investigated as well. Further wind tunnel experimental measurements are required to validate simulation cases with crosswinds. Because of the computational cost of running IDDES models with very fine grids, verification and validation (V&V) has not yet been conducted to estimate numerical and modelling errors and other associated uncertainties. V&V should be conducted on the basis of the framework developed by Xing [31], and the factor of safety method by Xing and Stern [32].

References

1. Corin, R.J., He, L. and Dominy, R.G., 2008. A CFD investigation into the transient aerodynamic forces on overtaking road vehicle models. *Journal of Wind Engineering and Industrial Aerodynamics*, *96*(8), pp.1390-1411.

2. Howell, J., Garry, K. and Holt, J., 2014. The Aerodynamics of a Small Car Overtaking a Truck. *SAE International Journal of Passenger Cars-Mechanical Systems*, *7*(2014 01-0604), pp.626-638.

3. Altinisik, A., Yemenici, O. and Umur, H., 2015. Aerodynamic analysis of a passenger car at yaw angle and two-vehicle platoon. *Journal of Fluids Engineering*, *137*(12), p.121107.

4. Moore, G.E., 1998. Cramming more components onto integrated circuits. *Proceedings of the IEEE*, *86*(1), pp.82-85..

5. Tsubokura, M., Kobayashi, T., Nakashima, T., Nouzawa, T., Nakamura, T., Zhang, H., Onishi, K. and Oshima, N., 2009. Computational visualization of unsteady flow around vehicles using high performance computing. *Computers & Fluids*, *38*(5), pp.981-990.

6. Tsubokura, M., Nakashima, T., Kitayama, M., Ikawa, Y., Doh, D.H. and Kobayashi, T., 2010. Large eddy simulation on the unsteady aerodynamic response of a road vehicle in transient crosswinds. *International Journal of Heat and Fluid Flow*, *31*(6), pp.1075-1086.

7. Sterken, L., Sebben, S., Walker, T. and Lofdahl, L., 2013. *Experimental and Numerical Investigations of the Base Wake on an SUV* (No. 2013-01-0464). SAE Technical Paper.

8. Wang, Y.R. and Cheng, Y.C., 2007. The Transient Flow Field Numerical Analysis of Vehicles Intersection for a Variety of Travel Spacing. *Journal of Flow Visualization and Image Processing*, *14*(2).

9. Al Homoud, S.S., Harmanto, D. and Oraifige, I., 2014. An Investigation into the Effect of Drag Coefficient on Overtaking of Car. In *Applied Mechanics and Materials* (Vol.493, pp. 151-154). Trans Tech Publications.

10. Zhang, Z., Zhang, Y.C. and Li, J., 2010. Vehicles aerodynamics while crossing each other on road based on computational fluid dynamics. In *Applied Mechanics and Materials* (Vol. 29, pp. 1344-1349). Trans Tech Publications.

11. Girimaji, S.S., 2006. Partially-averaged Navier-Stokes model for turbulence: A Reynolds averaged Navier-Stokes to direct numerical simulation bridging method. *Journal of Applied Mechanics*, *73*(3), pp.413-421.

12. Basara, B., Jakirlić, S., Aldudak, F. and Tropea, C., 2010. Truck Interference Effects on a Car during an Overtaking Manoeuvre: A Computational Study. *New Results in Numerical and Experimental Fluid Mechanics VII*, pp.611-619.

13. Pasala, K., Aȧ, B., Rao, H.J., Reddy, K.S. and Naidu, T.S., 2014. A CFD Investigation into the Flow Distribution on a Car passing by a Truck. *International Journal of Current Engineering and Technology*.

14. Schrefl, M., Mayer, J. and Tropea., C., 2006. On the Set-Up of a Surface Pressure Measurement System for On-Road Tests and Preliminary Results Concerning Highway-Passing Maneuvers. *6th MIRA International Conference on Vehicle Aerodynamics.*

15. Uystepruyst, D. and Krajnović, S., 2013. Numerical simulation of the transient aerodynamic phenomena induced by passing manoeuvres. *Journal of Wind Engineering and Industrial Aerodynamics*, *114*, pp.62-71.

16. Noger, C., Regardin, C. and Szechenyi, E., 2005. Investigation of the transient aerodynamic phenomena associated with passing manoeuvres. *Journal of fluids and structures*, *21*(3), pp.231-241.

17. Kremheller, A., 2015. Aerodynamic Interaction Effects and Surface Pressure Distribution during On-Road Driving Events. *SAE International Journal of Passenger Cars Mechanical Systems*, *8*(2015-01-1527), pp.165-176.

18. Blocken, B. and Toparlar, Y., 2015. A following car influences cyclist drag: CFD simulations and wind tunnel measurements. *Journal of Wind Engineering and Industrial Aerodynamics*, *145*, pp.178-186.

19. ANSYS Fluent Theory Guide, Release 17.1, April 2016.

20. Shur, M.L., Spalart, P.R., Strelets, M.K. and Travin, A.K., 2008. A hybrid RANS-LES approach with delayed-DES and wall-modelled LES capabilities. *International Journal of Heat and Fluid Flow*, *29*(6), pp.1638-1649.

21. Spalart, P.R., Deck, S., Shur, M.L., Squires, K.D., Strelets, M.K. and Travin, A., 2006. A Pnew version of detached-eddy simulation, resistant to ambiguous grid densities. *Theoretical and computational fluid dynamics*, *20*(3), pp.181-195.

22. Spalart, Philippe & Jou, W-H & Strelets, Michael & Allmaras, Steven. (1997). Comments on the Feasibility of LES for Wings, and on a Hybrid RANS/LES Approach.Strelets, M., 2001. Detached eddy simulation of massively separated flows. In 39th Aerospace sciences meeting and exhibit (p. 879).

23. Gritskevich, M.S., Garbaruk, A.V., Schütze, J. and Menter, F.R., 2012. Development of

DDES and IDDES Formulations for the k-ω Shear Stress Transport Model. *Flow, turbulence and combustion*, *88*(3), pp.431-449.

24. Menter, F.R., Kuntz, M. and Langtry, R., 2003. Ten years of experience with the SST turbulence model. Turbulence Heat Mass Transfer 4, 625–632.

25. Xing, T., 2014. Direct numerical simulation of Open Von Kármán Swirling Flow. *Journal of Hydrodynamics, Ser. B*, *26*(2), pp.165-177.

26. Kolář, V., 2007. Vortex identification: New requirements and limitations. *International journal of heat and fluid flow*, *28*(4), pp.638-652.

27. Holmén, V., 2012. Methods for Vortex Identification. In *Master's Thesis in Mathematical Sciences, FMA820 20121*. https://lup.lub.lu.se/studentpapers/search/publication/3241710

28. Sykes, D.M., 1973. Advances in Road Vehicle Aerodynamics. *BHRA Fluid Engineering*, Cranfield, UK, pp.311-321.

29. Stafford, L.G., 1981. A streamline wind-tunnel working section for testing at high blockage ratios. *Journal of Wind Engineering and Industrial Aerodynamics*, 9(1-2), pp.23-31.

30. Altinisik, A., Kutukceken, E. and Umur, H., 2015. Experimental and numerical aerodynamic analysis of a passenger car: Influence of the blockage ratio on drag coefficient. *Journal of Fluids Engineering*, 137(8), p.081104.

31. Xing, T., 2015. "A General Framework for Verification and Validation of Large Eddy Simulations." *Journal of Hydrodynamics, (Ser. B)*, 27(2): 163-175.

32. Xing, T. and Stern, F., 2010. "Factors of safety for Richardson extrapolation." *Journal of Fluids Engineering*, 132(6), p.061403.